Toxicology in Vitro 115 (2026) 106221

Contents lists available at ScienceDirect

Toxicology in Vitro

journal homepage: www.elsevier.com/locate/toxinvit

Harnessing human colonoid-derived monolayers as an *in vitro* platform for investigating accumulation, toxicity, and pharmacodynamics of small molecules

Pedro G.M. Canhão [a,c], Anny Smeuninx [c], Suzy Geerinckx [a], Raymond Evers [b], Jan Snoeys [a], Patrick Augustijns [c], Stephanie Kourula [a,*]

[a] Preclinical Sciences & Translational Safety, Johnson & Johnson, Turnhoutseweg 30, 2340 Beerse, Belgium
[b] Preclinical Sciences & Translational Safety, Johnson & Johnson, Spring House, Pennsylvania, USA
[c] Drug Delivery and Disposition, KU Leuven, Gasthuisberg O&N II, Herestraat 49 – Box 921, 3000 Leuven, Belgium

ARTICLE INFO

Editor: Maxime Culot

Keywords:
Drug accumulation
Drug-induced diarrhea
Human colonoid-derived monolayers
Intestinal toxicity
Pharmacodynamics
Prostaglandin

ABSTRACT

The purpose of this study was to evaluate differentiated human colonoid-derived monolayers (hCDMs) as an *in vitro* platform for investigating small molecule accumulation, toxicity, and pharmacodynamics (PD), in comparison to Caco-2 monolayers.

Differentiated hCDMs formed polarized monolayers with a physiological barrier function (332.1 ± 52.02 Ω × cm^2). In toxicity assays for drug-induced diarrhea, hCDMs demonstrated enhanced sensitivity to the epidermal growth factor receptor tyrosine kinase inhibitors (EGFR-TKIs) erlotinib and gefitinib, evidenced by lower concentrations inducing 20% inhibition (IC_{20}) of cell viability and $IC_{20}/30\times$ maximal plasma concentration (C_{max}) ratios, and decreased sensitivity to SN-38, indicated by higher IC_{20} and $IC_{20}/30\times$ C_{max}, compared to Caco-2 monolayers. Baseline eicosanome profiling showed that hCDMs provided a colon-like representation of the prostaglandin (PG) pathway, whereas Caco-2 monolayers displayed cancer-associated profiles, such as elevated $PGF_{2\alpha}$ and 15k $PGF_{2\alpha}$. Treatment with nonsteroidal anti-inflammatory drugs (NSAIDs) revealed that celecoxib elicited a dose-dependent reduction in the abundance of a subset of PGs within hCDMs, an effect not observed in the Caco-2 system.

In conclusion, hCDMs present a more physiologically relevant alternative to conventional Caco-2 monolayers for integrated studies of cellular accumulation, toxicity, and PD in the colon. Incorporating additional donors and a broader compound panel will further enhance understanding of the model's clinical relevance.

1. Introduction

Understanding the relationship between pharmacokinetics (PK; concentration versus time) and pharmacodynamics (PD; biological effect versus time) plays a vital role in pharmaceutical drug discovery and development (Lohasz et al., 2021; Tuntland et al., 2014). Prior to clinical trials, extensive preclinical studies evaluate the PK/PD properties of novel compounds (Li et al., 2019; Tuntland et al., 2014). This enables the design of treatment regimens that maximize therapeutic efficacy while minimizing safety risks (Hartung, 2024; Lohasz et al., 2021; Miller

Abbreviations: AA, Arachidonic acid; AE, Adverse effect; BCRP, Breast cancer resistance protein; BCS, Biopharmaceutics classification system; CIVMs, Complex *in vitro* models; C_{max}, Maximum plasma concentration; COX, Cyclooxygenase; CRC, Colorectal cancer; $C_{u,cell}$, Unbound intracellular drug concentration; DMEM, Dulbecco's modified Eagle's medium; DMET, Drug metabolizing enzyme and transporter; DPBS, Dulbecco's phosphate-buffered saline; EGFR-TKI, Epidermal growth factor receptor tyrosine kinase inhibitor; $f_{u,cell}$, Unbound drug fraction in the cell; GI, Gastrointestinal; hCDMs, Human colonoid-derived monolayers; HIO, Human intestinal organoid; IBD, Inflammatory bowel disease; IC_{20}, Concentration inducing 20% inhibition; IC_{50}, Half-maximal inhibitory concentration; LC, Liquid chromatography; MEM NEAA, Minimum essential medium non-essential amino acids; MoA, Mechanism of action; MoT, Mechanism of toxicity; MPS, Microphysiological systems; MS, Mass spectrometry; NAMs, New approach methodologies; NSAID, Nonsteroidal anti-inflammatory drug; ODM, Organoid differentiation medium; OGM, Organoid growth medium; P_{app}, Apparent permeability coefficient; PD, Pharmacodynamics; PG, Prostaglandin; P-gp, P-glycoprotein; PK, Pharmacokinetics; RED, Rapid equilibrium dialysis; ROCK, Rho-associated protein kinase; SI, Small intestine; TEER, Transepithelial electrical resistance.

* Corresponding author.
E-mail address: skourula@its.jnj.com (S. Kourula).

https://doi.org/10.1016/j.tiv.2026.106221
Received 12 November 2025; Received in revised form 20 February 2026; Accepted 4 March 2026
Available online 6 March 2026

et al., 2005). Yet, about 90% of potential drug candidates in clinical trials fail, with nearly 80% of these failures stemming from PK/PD-related issues, specifically insufficient efficacy (40–50%) and undetected toxicity (30%) (Khalil et al., 2020; Sun et al., 2022).

Assessments of drug efficacy, mechanism of action (MoA), and safety currently rely on distinct test systems (Monticello et al., 2017; Olson et al., 2000; Van Norman, 2019). Efficacy and MoA are typically studied through a combination of animal and *in vitro* models, whereas intestinal safety evaluations still mainly depend on animal studies (Hartung, 2024; Monticello et al., 2017; Morgan et al., 2013; Olson et al., 2000). Despite their widespread use, inherent species differences—such as variations in gut anatomy, function, drug metabolizing enzyme and transporter (DMET) composition, morphology, and lack of host genetic diversity and pharmacogenetics—hinder the translation of animal data to human outcomes (Hartung, 2024; Monticello et al., 2017). These disparities often lead to poor concordance between toxicities observed in animal models and adverse effects (AEs) in clinical settings, substantially contributing to drug attrition during trials (Monticello et al., 2017; Olson et al., 2000; Tamaki et al., 2013). Notably, positive predictive values for gastrointestinal (GI) AEs reveal low concordance in rodents (43%) and dogs (52%), but are markedly higher in non-human primates (91%) (Monticello et al., 2017). Consequently, there is an emerging demand for translatable *in vitro* models that accurately replicate drug candidate efficacy and toxicity (Hartung, 2024; Lohasz et al., 2021; Markus et al., 2021; O'Mahony et al., 2025).

The human colorectal adenocarcinoma-derived Caco-2 cell line has long been heralded as the gold standard for high-throughput screening (HTS) of drug absorption in the pharmaceutical industry, serving as a surrogate for the human intestinal barrier (Larregieu and Benet, 2013; Press and Di Grandi, 2008). However, its use in efficacy and toxicity studies remains comparatively limited (Kus et al., 2023). Notwithstanding its prevalent adoption, Caco-2 monolayers exhibit limited cellular complexity (e.g., absence of mucus-producing cells) (Panse and Gerk, 2022; Sun et al., 2008) and altered DMET expression (Englund et al., 2006; Müller et al., 2017; Ölander et al., 2016), as well as morphological and functional variability due to passage number and subclone heterogeneity (Sun et al., 2008).

A breakthrough occurred in 2011 when Sato and colleagues pioneered a method to isolate stem cells from the human intestine and grow them into 3D structures called human intestinal organoids (HIOs) (Sato et al., 2011). In contrast to Caco-2 cells, HIOs mimic epithelial physiology in a region-specific manner (Kraiczy et al., 2019) and maintain donor phenotypes for up to 17 passages (van der Hee et al., 2020). These organoids support long-term culture, expansion, and cryopreservation (d'Aldebert et al., 2020; Mahe et al., 2015; Sato et al., 2011; Sato et al., 2009; Zietek et al., 2020), and can be used in either proliferative (undifferentiated) or differentiated states, a feature especially valuable for assessing intestinal safety when the mechanism of toxicity (MoT) is unknown (Klein et al., 2025). Nevertheless, their spherical architecture and direction of polarization restrict access to the luminal (or apical) membrane, thereby limiting their utility in drug disposition studies and precluding easy assessment of barrier function, drug application, or luminal content sampling (Kwon et al., 2021; VanDussen et al., 2015). To overcome this hurdle, alternative strategies, including microinjection (Arian et al., 2024; O'Mahony et al., 2025), reversal of polarity to create apical-out 3D organoids (Arian et al., 2024; O'Mahony et al., 2025), or formation of Transwell®-based 2D monolayers, permitting access to both apical and basal surfaces (Ambrosini et al., 2020; Kourula et al., 2023; Kwon et al., 2021; VanDussen et al., 2015), have been employed.

Recent advances in stem cell technology have gained burgeoning attention, spurring the development of physiologically relevant human complex *in vitro* models (CIVMs) that can enhance the preclinical evaluation of drug candidates over traditional animal and *in vitro* systems (Cirit and Stokes, 2018; Ekert et al., 2020). HIOs, derived from $LGR5^{+}$ crypt base columnar stem cells (Pleguezuelos-Manzano et al., 2020; Sato et al., 2011) or induced pluripotent stem cells (iPSCs) (Finkbeiner et al., 2015; Yoshida et al., 2020), alongside human intestinal microtissues (Ayehunie et al., 2018; Canhão et al., 2025) and gut-on-chip microphysiological systems (MPS) (Hartung and Smirnova, 2025; Signore et al., 2021; Steinway et al., 2020), hold promise for improving early compound selection by identifying drugs with desirable intestinal safety profiles, reducing reliance on animal testing, and bridging interspecies differences to better assess the human relevance of animal-derived toxicity data (Vandana et al., 2023).

Intestinal toxicity is the most common category of AEs observed in Phase 1 clinical trials and post-approval, manifesting as diarrhea, nausea, vomiting, constipation, and abdominal pain (Federer et al., 2016; Monticello et al., 2017; Peters et al., 2020). Often, these AEs remain undetected until later stages of drug development during clinical trials. Ideally, they would be identified and addressed preclinically to evaluate drug safety profiles, optimize dosing regimens, and mitigate potential harm to trial participants (Eaton et al., 2016). Despite the high incidence in clinical trials, intestinal toxicity rarely (<10%) leads to drug attrition, frequently requiring symptom management that diminishes patient compliance, potentially sacrificing efficacy, and increasing treatment costs (Clark and Steger-Hartmann, 2018). In current programs, intestinal safety assessments depend on animal models, which are ill-suited for HTS and restrict large-scale drug testing (Hartung, 2024; Li et al., 2019). Landmark studies underscore the need for incorporating non-rodent, higher-order species to enhance the translatability of preclinical findings to human AEs (Monticello et al., 2017; Olson et al., 2000). However, ethical and financial constraints often limit testing in these species to the final candidate drug (Monticello et al., 2017). Thus, innovative assays using CIVMs may effectively bridge this animal-human translation gap.

So far, the main focus of gut CIVMs has been on the upper GI tract, as approximately 90% of orally administered marketed drugs are absorbed in the small intestine (SI) (Pretorius and Bouic, 2009). Given the pivotal medical and societal impact of local disorders like colorectal cancer (CRC) and inflammatory bowel disease (IBD) (Hammer and Langholz, 2020; Marcellinaro et al., 2024), there is a growing need to create CIVMs that elucidate colonic drug disposition and enhance the development of new colon-targeting formulations for local drug delivery (Canhão et al., 2025).

Achieving adequate drug concentration at the intracellular target site is crucial for therapeutic efficacy; insufficient accumulation can result in subpar efficacy, whereas excessive intracellular levels may induce toxicity (Mateus et al., 2017; Riccardi et al., 2016). This balance is pertinent for effective treatment of CRC and IBD, which require sufficient drug accumulation within the colonic epithelium to ensure higher concentrations in diseased tissues while limiting systemic exposure (Tannergren et al., 2009). Evidence from epidemiological, preclinical, and clinical studies suggests that long-term use of nonsteroidal anti-inflammatory drugs (NSAIDs) can reduce CRC risk. NSAIDs inhibit cyclooxygenase (COX) enzymes, leading to a reduction in prostaglandin (PG) levels (Maniewska and Jeżewska, 2021). According to the free drug theory, the pharmacologically relevant concentration for targets located inside the cell driving the PD response is the unbound intracellular drug concentration ($C_{u,cell}$), rather than the total cellular concentration (C_{cell}), as only free drug molecules can interact with the target (Mateus et al., 2017; Mateus et al., 2013; Riccardi et al., 2018; Treyer et al., 2019). Therefore, quantifying $C_{u,cell}$ is paramount to better predict drug efficacy and toxicity (Mateus et al., 2017; Treyer et al., 2018).

This study investigates differentiated human colonoid-derived monolayers (hCDMs) as a proof-of-concept to harness drug accumulation, toxicity, and PD, in comparison to Caco-2 monolayers. Human SI—such as proliferative 3D ileal organoids, proliferative and differentiated 3D duodenal organoids, and EpiIntestinal™ microtissue (Belair et al., 2020; Klein et al., 2025; Peters et al., 2019)—along with colon-derived CIVMs like RepliGut® Planar (proliferative and differentiated monolayers) (Pike et al., 2025) have been deployed to predict drug-induced diarrhea. Building upon this and our previous work with

proliferative human 3D duodenal and colonic organoids (Kourula et al., 2023), we evaluated toxicity responses of hCDMs and Caco-2 monolayers to six marketed small molecules associated with varying clinical diarrhea incidence. The concentration inducing 20% inhibition (IC_{20}) of cell viability for each drug was benchmarked against its corresponding human clinical maximum plasma concentration (C_{max}) to assess the diarrheagenic risk. The unbound counterparts ($IC_{20,u}$ and $C_{max,u}$) were estimated to account for binding effects on exposure. Furthermore, we determined $C_{u,cell}$ (and C_{cell}) for the NSAIDs celecoxib and sulindac. Finally, the ability of hCDMs (versus Caco-2 monolayers) to capture PD was explored by profiling their eicosanome (127 eicosanoids, emphasizing a subset of PGs) at baseline and post-NSAID treatment.

2. Materials and methods

2.1. Chemicals and reagents

Gefitinib, irinotecan (CPT-11), SN-38, sulindac sulfone, elacridar (GF120918), and tolbutamide were obtained from Sigma-Aldrich (Overijse, Belgium). Erlotinib, celecoxib, sulindac, and sulindac sulfide were provided by Johnson & Johnson Innovative Medicine (Beerse, Belgium). Hydroxycelecoxib and SN-38 glucuronide (SN-38-G) were purchased from Santa Cruz Biotechnology, Inc. (Dallas, TX, USA). [^{3}H] digoxin, [^{14}C]mannitol, and Ultima Gold™ Liquid Scintillation Cocktail were acquired from Revvity Health Sciences (Waltham, MA, USA). A total of 127 arachidonic acid (AA)-derived eicosanoids, along with 40 deuterium-labeled internal standards (IS), were sourced from Cayman Chemical (Ann Arbor, MI, USA).

IntestiCult™ Human Organoid Growth Medium (OGM) and IntestiCult™ Human Organoid Differentiation Medium (ODM) were purchased from STEMCELL Technologies (Vancouver, Canada). The rho-associated protein kinase (ROCK) inhibitor Y-27632 dihydrochloride was procured from Tocris Bioscience (Bristol, UK), and Matrigel® matrix from Corning Life Sciences (Bedford, MA, USA).

Dulbecco's phosphate-buffered saline with Ca^{2+} and Mg^{2+} ($DPBS^{++}$), Dulbecco's phosphate-buffered saline without Ca^{2+} and Mg^{2+} (DPBS), Hanks' balanced salt solution (HBSS), Dulbecco's modified Eagle's medium (DMEM), Dulbecco's modified Eagle's medium/Ham's F-12 nutrient mixture (Advanced DMEM/F12), minimum essential medium non-essential amino acids (MEM NEAA), fetal bovine serum (FBS), penicillin/streptomycin (Pen/Strep), GlutaMAX™, L-glutamine, and TrypLE™ Express were all supplied by Thermo Fisher Scientific (Gibco™; Merelbeke, Belgium). Bovine serum albumin (BSA), butylated hydroxytoluene (BHT), ethylenediaminetetraacetic acid (EDTA), Trypsin-EDTA solution, and 4-(2-hydroxyethyl)-1-piperazineethanesulfonic acid (HEPES) were sourced from Sigma-Aldrich (Overijse, Belgium).

Dimethyl sulfoxide (DMSO), methanol (MeOH), acetic acid, formic acid, and the ultrapure water system Milli-Q® IQ 7000 with Millipak® 0.22 µm hydrophilic membrane filter were acquired from Merck KGaA (Darmstadt, Germany). Acetonitrile was obtained from Biosolve Chimie (Dieuze, France) and isopropanol from VWR Chemicals (Amsterdam, The Netherlands). All solvents were of analytical grade.

All other reagents utilized in the methods described are detailed in their respective sections below.

2.2. In vitro systems

2.2.1. Human tissue source

An established line of healthy human colon organoids was obtained from the Foundation Hubrecht Organoid Biobank (Utrecht, the Netherlands). These colonoids were derived from the ascending colon of a 42-year-old female donor (HUB-02-D2-089, lot number: W21-50018). All experiments described in this work were conducted using this donor. All material was obtained under a Medical Ethics Review Committee (Medisch Ethische Toetsingscommissie, METC) and Biobank Review Committee (Toetsingscommissie Biobanken, TCBio) approved protocol from human intestinal tissue and University Medical Center (UMC) Utrecht HUB-STEM protocol. Experimental procedures involving this organoid line adhered to prior informed patient consent for the study and HUB-STEM protocol, as well as data protection and pseudonymization.

2.2.2. Human 3D colonoid culture

For this study, human cystic-like colonoids between passages 12 to 16 were maintained in proliferation. Previously cryopreserved colonoids were thawed, embedded in Matrigel® (Corning Life Sciences, #356231, lot number: 2285001), and expanded in IntestiCult™ Human Organoid Growth Medium (OGM; STEMCELL Technologies, #06010), supplemented with 1% Pen/Strep (Gibco™, #15070-063). During the first 2 days of culture and the 2 days after passaging, 10 µM ROCK inhibitor (Y-27632; Tocris Bioscience, #1254) was added to the expansion medium.

Passaging occurred every 5 to 8 days, whereby colonoids were collected in ice-cold Advanced DMEM/F12 (Ad-DF; Gibco™, #1263401) with 1% Pen/Strep, 1% GlutaMAX™ (Gibco™, #35050061), 10 mM HEPES (Gibco™, #15630080)—hereinafter referred to as AD-DF +/+/+—and 1% BSA (Sigma-Aldrich, #9048-46-8). The colonoids were mechanically disrupted using a pre-wetted P1000 pipette tip followed by a P200 tip, or pre-wetted fire-polished Pasteur pipettes, at a split ratio of 1:3. The resulting cell suspension was pelleted by centrifugation (220 × g for 5 min at 4 °C) and subsequently resuspended in ice-cold 70% Matrigel® in IntestiCult™ OGM containing 1% Pen/Strep and 10 µM ROCK inhibitor. Hemispherical droplets (or domes) of 10 µL of this cell suspension were then plated onto pre-warmed Costar® 6-well plates (Corning Life Sciences, #3471), ensuring that each well contained 15 to 20 domes. The plates were inverted and incubated at 37 °C in a humidified environment with 5% CO_2, allowing the Matrigel® to solidify. After 1h, pre-warmed medium was added, with medium renewal occurring every 2 to 3 days at a volume of 3 mL/well. Brightfield images were captured every 2 to 3 days using standardized acquisition settings on the EVOS™ M5000 Imaging System (Thermo Fisher Scientific).

2.2.3. Human 2D colonoid-derived monolayer (hCDM) seeding and establishment

Colonoids were passaged through mechanical disruption 5 days prior to monolayer preparation, as outlined in Section 2.2.2. On day 5 post-passaging, colonoids, cultivated in 10 µL domes, were collected in AD-DF +/+/+ containing 1% BSA, triturated repeatedly to disrupt Matrigel®, centrifuged (220 × g for 5 min at 4 °C), and the medium and most of the Matrigel® were aspirated. Colonoid pellets were then suspended in 1 mL of TrypLE™ Express (Gibco™, #12604013) with 10 µM ROCK inhibitor per 15 mL tube. This mixture was incubated at 37 °C, vortexed and monitored under the microscope every 2 min until colonoids were digested to single cells. Single cells were resuspended in 12 mL AD-DF +/+/+ with 1% BSA and centrifuged (450 × g for 5 min at 4 °C) to wash out residual TrypLE™. The final cell suspension was prepared in IntestiCult™ OGM, supplemented with 1% Pen/Strep and 10 µM ROCK inhibitor.

Simultaneously, Matrigel® was diluted 40x in ice-cold $DPBS^{++}$ (Gibco™, #14040091) and used to coat the surface of 96-well cell culture inserts (Corning® HTS Transwell®-Polyester, PET; 0.4 µm, 0.143 cm^2) for at least 1h at 37 °C. After coating period, the Matrigel® solution was aspirated, and the inserts were washed twice with room temperature $DPBS^{++}$ before the cell suspension was plated. Subsequently, 300 µL of IntestiCult™ OGM supplemented with 1% Pen/Strep and 10 µM ROCK inhibitor was pipetted in the basolateral compartment of the inserts. 150 µL of cell suspension at a density of 3.5 x 10^5 cells/cm^2 (5 x 10^4 cells/insert) was seeded into the apical compartment. Plates were incubated at 37 °C and 5% CO_2, with expansion medium refreshed 3 times per week.

hCDMs were maintained in expansion medium until the

transepithelial electrical resistance (TEER) reached 100 Ω × cm^2, as noted in prior studies (Jelinsky et al., 2023; Kourula et al., 2023; Parente et al., 2024). Differentiation was induced by replacing IntestiCult™ OGM with IntestiCult™ Human Organoid Differentiation Medium (ODM; STEMCELL Technologies, #100-0214). hCDMs were then cultured in differentiation medium for up to 5 days before initiating experiments, which took place on day 4 or 5 of differentiation. Medium was refreshed every 2 to 3 days, and brightfield images of hCDMs were captured every 2 to 3 days using the EVOS™ M5000 Imaging System (Thermo Fisher Scientific).

2.2.4. Caco-2 monolayer culture

Caco-2 monolayers were prepared as previously described (Canhão et al., 2025; Kourula et al., 2023), with slight modifications made to the protocol. Caco-2 cells (ATCC, HTB-37™, lot number: 7001334) were obtained from the American Tissue Culture Collection (Rockville, MD, USA). For this study, cells within a low passage interval (23−27) were utilized. Following thawing, cells were plated in T-75 tissue culture flasks (VWR®, Radnor, PA, USA) and incubated at 37 °C, 5% CO_2 and 95% relative humidity. Cells were harvested with trypsin-EDTA, counted, and seeded at a density of 8.2 x 10^4 cells/cm^2 onto 96-well cell culture inserts (Millicell®-Polycarbonate, PCF; 0.4 μm, 0.11 cm^2). 75 μL of cell suspension was seeded into the apical compartment, and 250 μL of culture medium was pipetted in the basolateral compartment. The medium consisted of DMEM (Gibco™, #41965-039) supplemented with 20% FBS (Gibco™, #10270-106), 1% MEM NEAA (Gibco™, #11140-035), 1% L-glutamine (Gibco™, #25030-024) and 2% Pen/Strep (Gibco™, #15070-063) and was replaced one day after seeding and every 2 to 3 days thereafter. After 21 days of culture, the Caco-2 monolayers were used for the subsequent experiments.

2.3. Model characterization

2.3.1. Protein determination

Total protein concentration was determined using the bicinchoninic acid (BCA) method with the Pierce™ BCA Protein Assay Kit (Thermo Fisher Scientific, #23227), according to the manufacturer's protocol. Absorbance was measured at 562 nm with a Tecan Spark® 10M High Performance Multi-Mode Microplate Reader (Männedorf, Switzerland).

2.3.2. Transepithelial electrical resistance (TEER) measurements

TEER was employed to evaluate tissue integrity within each insert of both hCDMs and Caco-2 monolayers. Measurements were performed using an EVOM™ Auto TEER Measurement System (World Precision Instruments, #EVA-MT-03) equipped with a 96-well HTS electrode array, and all readings were taken on a heating plate set to 37 °C.

TEER values, reported in Ω x cm^2, were calculated by subtracting the resistance of an empty insert from the recorded raw resistance measurements and subsequently multiplying the resulting value by the surface area of the respective tissue culture insert (0.143 cm^2 for hCDMs and 0.11 cm^2 for Caco-2).

For toxicity evaluations, TEER was assessed every 24h and normalized to DMSO-treated (0.5%) vehicle controls. Relative TEER (% control) was determined by dividing the TEER of treated tissues by that of vehicle control tissues, multiplied by 100. For drug transport experiments, TEER assessments were systematically conducted both before ($TEER_{pre\text{-}assay}$) and after ($TEER_{post\text{-}assay}$) the assay.

TEER of hCDMs was closely monitored throughout the expansion and differentiation phases until culture endpoints. Once the threshold of 100 Ω × cm^2 was reached, the expansion medium was replaced with IntestiCult™ ODM to induce differentiation, as detailed in Section 2.2.3. For Caco-2, TEER was measured on day 21, and only wells with TEER values ≥ 195 Ω x cm^2 were selected for further analyses (Hubatsch et al., 2007).

2.3.3. Liquid chromatography–tandem mass spectrometry (LC–MS/MS) analysis

Samples obtained from PD and cell accumulation studies with hCDMs and Caco-2 monolayers were analyzed using LC–MS/MS to quantify 127 eicosanoids along with 2 NSAIDs: celecoxib and sulindac.

Each sample was diluted 1:1 with DMSO and dispensed into 96-deep well plates containing 5 μL of an antioxidant mixture (0.2 mg/mL BHT/EDTA in MeOH/water; 1:1 v/v). A combined stock solution of the eicosanoid standards (127 eicosanoids) was prepared by adding 10 μg of each eicosanoid to a glass tube and bringing the total volume to 10 mL with MeOH, resulting in a final concentration of 1 μg/mL for each component. Serial dilutions were made in MeOH to achieve a concentration range of 0.1–1000 ng/mL. A stock solution of deuterated (d_4-d_{11}) internal standards (40 IS) was prepared by adding 5 μg of each labeled eicosanoid to a glass container to obtain a final concentration of 500 ng/mL per standard. For each batch, a 1:10 dilution in MeOH was made from this stock. Calibration standard samples were prepared by spiking blank matrix with the calibration solutions. The same volume of blank MeOH was added to the study samples. Both calibration standards and study samples were processed concurrently. The mixtures were diluted with 10% MeOH in water to 0.5 mL, and the IS mixture was added immediately. All samples were vortexed and centrifuged at 5000-6000 × g for 10 min. Due to limited sample availability, 100 μL of the supernatant was used for celecoxib and sulindac analysis. The remaining sample underwent solid-phase extraction (SPE) using Strata-X 33-μm polymeric reversed phase 96-well plates (60 mg/well; Phenomenex, Torrance, CA, USA) (Song et al., 2013).

Calibration solutions for celecoxib and sulindac were prepared through serial dilutions in blank DMSO. Calibrations standards were prepared by spiking blank matrix with the calibration solutions, and the same volume of blank DMSO was added to the supernatant of the study samples. Acetonitrile containing tolbutamide as a general IS was added, followed by vortexing and centrifugation. The supernatant was then injected into the liquid chromatography (LC) system for analysis.

Sample preparation for analytes used in transport studies across Caco-2 monolayers (erlotinib, gefitinib, irinotecan, SN-38, SN-38-G, celecoxib, hydroxycelecoxib, sulindac, sulindac sulfide, and sulindac sulfone) followed a methodology akin to that used for celecoxib and sulindac.

2.3.4. Liquid chromatography (LC) optimization

Chromatographic separation from matrix interferences and metabolites was conducted on a Nexera Ultra High-Performance Liquid Chromatography (UHPLC) system (Shimadzu) equipped with either a reversed-phase UHPLC column (Waters) or a Kinetex C18 column (Phenomenex). Optimized LC conditions for quantifying eicosanoids and NSAIDs are outlined in *Supplementary Table 1* (Appendix B.1, Table S1).

For chromatographic separation, extracted samples were injected onto the appropriate column (Table S1) operated at 50 °C, using the UHPLC system (Shimadzu).

Eicosanoids were eluted using mobile phases consisting of water/acetonitrile/acetic acid (70:30:0.1 v/v/v; mobile phase A) and acetonitrile/isopropanol/acetic acid (50:50:0.02 v/v/v; mobile phase B), following the gradient program specified by Song and colleagues (Song et al., 2013). Celecoxib and sulindac separation was also achieved via gradient elution, starting with 95% aqueous mobile phase (mobile phase A) and increasing the percentage of acetonitrile (mobile phase B) to 70% within 0.3 min, reaching 98% in 1.3 min, followed by a column wash and return to initial conditions, with a total run time of 2.5 min.

2.3.5. Mass spectrometry (MS) optimization

Mass spectrometric detection was carried out using a Triple Quadrupole 6500+ instrument (Sciex, Framingham, USA) operated in negative ion mode for eicosanoids and NSAIDs, whereas compounds tested in drug transport assays were analyzed in either positive or negative ion

mode, depending on the analyte. Fragmentation parameters were fine-tuned for each analyte's quantification, including tolbutamide, which served as a general IS for celecoxib and sulindac.

Quantification was achieved via scheduled multiple reaction monitoring (sMRM) in negative ion mode for all eicosanoids and NSAIDs, according to previously reported parameters (Song et al., 2013). For the remaining analytes, MS was operated in positive ion mode utilizing the TurboIonSpray™ interface (electrospray ionization) for erlotinib, gefitinib, irinotecan, SN-38, SN-38-G, and sulindac. Conversely, celecoxib, hydroxycelecoxib, sulindac sulfide, and sulindac sulfone were analyzed in negative ion mode. All MS parameters are comprehensively listed in *Supplementary Table 2* (Appendix B.1, Table S2) for eicosanoids and NSAIDs, and in *Supplementary Table 3* (Appendix B.1, Table S3) for compounds used in drug transport studies.

2.3.6. Sample analysis

Quantification of all 127 eicosanoids was performed automatically in all samples during a single run using an R-based software package (Song et al., 2013).

A log-log transposed linear regression model was applied for the other compounds. The peak area ratios of the analyte to its internal standard were plotted against the analyte concentrations. Sample concentrations were calculated by interpolation from the standard curves. The linearity of the instrument's response was validated through the back-calculated concentrations of the calibration samples, with calibration standard accuracies falling within 25% accuracy, and 30% accuracy at the lower limit of quantification (LLOQ).

2.3.7. Cellular drug binding

The homogenate was prepared by suspending a pellet of Caco-2 cells in HBSS buffered with 10 mM HEPES at pH 7.4 (dialysis buffer) to achieve a concentration of 20 x 10^6 cells/mL. The suspension was homogenized by sonication using a Vibra-Cell® VCX-130PB Ultrasonic Liquid Processor (Sonics & Materials, Newton, CT, USA) at 40% intensity for 30 s.

To maximize throughput, the assay was performed by cassette-dosing 2 compounds at a time. Cassette-dosing solutions were prepared by mixing equal volumes from a 200 μM intermediate concentration of each compound, resulting in a final concentration of 100 μM per compound in the cassette. This solution was spiked into each cell homogenate, yielding a final testing concentration of 1 μM for celecoxib, sulindac, erlotinib, and gefitinib. Lopinavir at 1 μM was included as a control for high binding.

Equilibrium dialysis was conducted in a Rapid Equilibrium Dialysis (RED) device (Thermo Fisher Scientific, #99006). Compound-spiked homogenates were added in triplicate to the donor (homogenate) side (300 μL), with blank dialysis buffer added to the receiver (buffer) side (500 μL) of the RED device. The dialysis unit was incubated at 37 °C on an orbital shaker set to 250 rpm for 6h. Equilibrium was confirmed by concurrently conducting dialysis experiments with the same cassette-dosed compounds spiked in blank dialysis buffer and dialyzing against the same blank dialysis buffer in the receiver side. Equilibrium was reached when the free fraction in buffer was ≥80%.

At the end of the incubation, 50 μL samples were collected from both donor and receiver chambers. Blank dialysis buffer or blank (unspiked) cell homogenate (50 μL) was added to the samples from the donor or receiver, respectively, to yield identical matrices. Compounds were extracted with MeOH containing 0.5 μM tolbutamide as an internal standard, and the extracted samples were centrifuged for 10 min at 2000 × g. The resulting supernatants were filtered through Impact™ 96-well protein precipitation plates (Phenomenex, #CE0-9344) into SiliGuard™ 96-well low binding collection plates (Analytical Sales and Services, #59623-23GC). Compound concentrations in the supernatant were quantified via LC–MS/MS.

Optimized LC and MS parameters for quantifying drug binding in Caco-2 cell homogenates are summarized in *Supplementary Table 4* (Appendix B.1, Table S4) and *Supplementary Table 5* (Appendix B.1, Table S5), respectively.

2.3.8. Bidirectional drug transport studies

Drug transport assays were performed as previously described (Canhão et al., 2025), with minor modifications. Caco-2 monolayers at day 21 were washed twice with HBSS (containing Ca^{2+} and Mg^{2+}) supplemented with 10 mM HEPES (pH 7.4) on both apical and basolateral sides (transport medium). Experiments were initiated by applying transport medium containing test drugs into either the apical or basolateral compartment (donor), depending on the transport direction under investigation, while the receiver compartment was filled with transport medium with 0.5% DMSO (150 μL apical and 150 μL basolateral). For drugs known to be substrates for specific transporters—such as gefitinib and erlotinib for multidrug resistance protein 1/P-glycoprotein (MDR1/P-gp) and breast cancer resistance protein (BCRP), as well as digoxin for MDR1/P-gp—experiments were conducted both in the presence and absence of the P-gp and BCRP inhibitor elacridar at 5 μM. Final concentrations in the donor compartment were 10 μM for erlotinib, gefitinib, and irinotecan, whereas celecoxib, sulindac, and [^{3}H]digoxin were tested at 1 μM. Monolayers were incubated at 37 °C in a humidified incubator with 5% CO_2. Each experimental condition was assessed in triplicate, with transport measurements carried out in both apical-to-basolateral (AP→BL) and basolateral-to-apical (BL→AP) directions for all drugs.

Prior to initiating the experiments, starting solutions of each test drug were sampled to verify their initial concentrations (C_{t0}). Subsamples were collected from both apical and basolateral sides at 30 and 60 min. At the end of the incubation period (120 min), samples were taken from both donor and receiver compartments to evaluate compound recovery. The concentrations of [^{3}H]digoxin and [^{14}C]mannitol were determined by liquid scintillation counting (LSC). Radiolabeled samples were mixed with 4 mL of Ultima Gold™ liquid scintillation cocktail in liquid scintillation vials, and radioactivity was measured with a Tri-Carb 4910TR liquid scintillation counter (Revvity Health Sciences, Waltham, MA, USA). All other compounds were analyzed by LC–MS/MS.

Barrier integrity of the treated models was evaluated by co-administering the test drug with 1 μM [^{14}C]mannitol to the donor side and measuring TEER, as described in Section 2.3.2. Only wells that maintained TEER values ≥ 50% of their starting value by the end of the transport experiment, along with a [^{14}C]mannitol apparent permeability coefficient (P_{app}) of ≤ 3.0 x 10^{-6} cm/s, were included in the study (Canhão et al., 2025; Kourula et al., 2023).

2.4. Compound selection

As shown in Table 1, the selection encompassed six reference small molecules with distinct PK/PD and toxicity characteristics across various drugs classes: erlotinib and gefitinib (epidermal growth factor receptor tyrosine kinase inhibitors, EGFR-TKIs); irinotecan and SN-38 (antineoplastics agents); and celecoxib and sulindac (NSAIDs).

Selection criteria accounted for positive or diarrheagenic drugs (e.g., erlotinib, gefitinib, irinotecan, and SN-38), hereafter defined as those with a clinical diarrhea incidence >25% and/or a black box warning for intestinal side effects (e.g., SN-38), alongside negative or non-diarrheagenic drugs (e.g., celecoxib and sulindac), denoting a diarrhea incidence of 0-5% (Belair et al., 2020; Peters et al., 2019).

Erlotinib, gefitinib, irinotecan and SN-38 (all diarrheagenic) are recognized as substrates for P-gp (Honeywell et al., 2020; Parvez et al., 2021; Xu and Li, 2019). Additionally, erlotinib and gefitinib are substrates for BCRP (Honeywell et al., 2020). Inhibition of P-gp and/or BCRP efflux using elacridar can enhance the intracellular concentration of these compounds, thereby increasing their *in vitro* exposure and cytotoxicity (Van Tellingen, 2001). This concept was investigated for irinotecan in hCDMs and for erlotinib and gefitinib in Caco-2

Table 1
Physicochemical properties and PK/PD/Tox characteristics of the studied compound set.

Compound	Drug Class	BCS Class	Drug Transporters[a]	Relevant Metabolites[b]	PD[c]	Reported Tox[d]
Erlotinib	EGFR-TKI	II	MDR1/P-gp; BCRP	*n.a.*	Interaction with EGFR ATP binding pocket	Diarrheagenic [+]
Gefitinib	EGFR-TKI	II	MDR1/P-gp; BCRP	*n.a.*	Interaction with EGFR ATP binding pocket	Diarrheagenic [+]
Irinotecan (CPT-11)	Antineoplastic (TOP1 inhibitor)	II	MDR1/P-gp	SN-38; SN-38-G	DNA damage (γ-H2AX induction) through TOP-1 inhibition	Diarrheagenic [+]
SN-38	Antineoplastic (TOP1 inhibitor)	IV	MDR1/P-gp	SN-38-G	DNA damage (γ-H2AX induction) through TOP-1 inhibition	Diarrheagenic [+]
Celecoxib	NSAID	II	*n.a.*	Hydroxycelecoxib; carboxycelecoxib; celecoxib glucoronide	Eicosanoid synthesis inhibitor (COX-2 selective or coxib)	Non-diarrheagenic [−]
Sulindac	NSAID	II	*n.a.*	Sulindac sulfide; sulindac sulfone	Eicosanoid synthesis inhibitor (non-selective COX)	Non-diarrheagenic [−]

BCRP – Breast cancer resistance protein, BCS – Biopharmaceutics classification system, COX-2 – Cyclooxygenase-2, EGFR – Epidermal growth factor receptor, MDR1/P-gp – Multidrug resistance protein 1/P-glycoprotein, NSAID – Non-steroidal anti-inflammatory drug, PD – Pharmacodynamics, PK – Pharmacokinetics, SN-38-G – SN-38 glucuronide, TKI – Tyrosine kinase inhibitor, and TOP1 – DNA topoisomerase 1. *n.a.* indicates not applicable.

[a] Sourced from Honeywell et al. (2020), Parvez et al. (2021), and Xu and Li (2019).

[b] Extracted from Brunell et al. (2011), Gong et al. (2012), and Xu and Villalona-Calero (2002).

[c] Obtained from Barbier et al. (2023), Calvo et al. (2007), Gong et al. (2012), Posadas et al. (2007), Tinsley et al. (2009), and Williams et al. (2000).

[d] Diarrheagenic [+] drugs were defined as those eliciting >25% incidence of diarrhea in the clinic and/or carrying a black box warning for intestinal side effects, whereas non-diarrheagenic [−] elicited a 0-5% clinical incidence of diarrhea, as adapted from the works of Belair et al. (2020), Kourula et al. (2023), and Peters et al. (2019). % diarrhea incindence linked to each compound is summarized in Table 2 (refer to diarrheagenic classification, DC).

monolayers.

Moreover, irinotecan is a pro-drug that is hydrolyzed to its primary active (cytotoxic) metabolite, SN-38, by carboxylesterase 2 (CES2) in enterocytes. This metabolite undergoes further metabolism via glucuronidation by UGT1A1 to its inactive form, SN-38-G (Parvez et al., 2021; Teft et al., 2015). The slower glucuronidation rate of SN-38 compared to its efficient formation by CES2 is the pivotal mechanism contributing to its intestinal accumulation (Smith et al., 2006). Thus, the therapeutic window of irinotecan arises from the interplay between P-gp-mediated efflux and metabolic processes, with its associated diarrheagenicity stemming from intestinal epithelial toxicity. The impact of these factors was assessed in hCDMs and Caco-2 monolayers.

Celecoxib and sulindac were chosen for their non-diarrheagenic properties and differentiable, measurable PD effects. Their anti-inflammatory action stems from inhibiting eicosanoid, particularly PG synthesis, through the inhibition of COX enzymes (Gong et al., 2012; Yin et al., 2016).

2.5. Toxicity testing

2.5.1. Assay criteria

Classifying drugs solely by their half-maximal inhibitory concentration (IC_{50}) is an insufficient metric for predicting clinical toxicity (Belair et al., 2020; Klein et al., 2025; Lin and Will, 2012). Incorporating human clinical C_{max} values significantly enhances the predictivity of *in vitro* assays for organ-specific toxicities (Lin and Will, 2012).

To relate our findings to clinical outcomes, the IC_{20} obtained in hCDMs and Caco-2 monolayers for each drug was normalized to the corresponding C_{max}. A safety margin of 30× C_{max} (Belair et al., 2020; Klein et al., 2025; Kourula et al., 2023) was applied to differentiate between the diarrheagenic and non-diarrheagenic drugs discussed in Section 2.4. Compounds were ranked by their $IC_{20}/30\times C_{max}$ ratio, with those having an $IC_{20}/30\times C_{max} < 1$ classified as assay positives. The use of IC_{20} (in place of IC_{50}) enabled the quantification of activity for compounds exhibiting less than 50% inhibition at the highest tested concentration (Peters et al., 2019; Pike et al., 2025). Clinical C_{max} in patients, following the first therapeutic dose, was sourced from published literature and/or FDA public databases. As a conservative approach, the highest reported clinical C_{max} was used to normalize the IC_{20} determined for each drug in hCDMs and Caco-2 monolayers.

2.5.2. Compound dose-response

Toxicity testing was conducted on differentiated hCDMs at day 15 (day 4 of differentiation) and Caco-2 monolayers at day 21, cultured following the protocols detailed in the cell culture section. All experiments were carried out in 96-well plates.

To accommodate a top dose of 30× C_{max}, all compounds were applied to the monolayers at a final DMSO concentration of 0.5%. Compounds were diluted in IntestiCult™ ODM with 1% Pen/Strep (hCDM vehicle control) or in DMEM supplemented with 20% FBS, 1% MEM NEAA, 1% L-glutamine, and 2% Pen/Strep (Caco-2 vehicle control), both containing 0.5% DMSO. These were then administered in half-log (3.16-fold) dilution series across 5-6 concentrations, at 150 µL/well. Both the apical and basolateral surfaces were treated to ensure maximal exposure. The final experimental conditions for the toxicity assessments are summarized in *Supplementary Table 6* (Appendix B.1, Table S6). Monolayers were incubated for 72h without further medium or compound replenishment. TEER was assessed every 24h to monitor monolayer integrity and normalized to DMSO-treated (0.5%) vehicle controls, as described in Section 2.3.2. Additionally, cultures were imaged every 24h using brightfield microscopy with the EVOS™ M5000 Imaging System (Thermo Fisher Scientific) to perform a visual quality control.

2.5.3. Cell viability assay

After 72h, cell viability was measured using an ATP-based viability assay (CellTiter-Glo® 2.0 Assay; Promega, #G9241). The CellTiter-Glo® reagent was diluted 1:1 with DPBS. Medium was removed, and 150 µL of the diluted reagent was added to each apical chamber and incubated with gentle shaking (150 rpm) for 1h at room temperature, shielded from light. Subsequently, 100 µL from each well were transferred to a White Opaque 96-Well Microplate (Thermo Fisher Scientific, #15042). Luminescence was recorded with EnVision HTS XCite Multimode Plate Reader (Revvity Health Sciences, Waltham, MA, USA). Luminescence in each condition was normalized to the corresponding on-plate DMSO-treated (0.5%) vehicle control.

2.6. Pharmacodynamics (PD) and cell accumulation

PD and cell accumulation studies were performed on differentiated hCDMs at day 16 (day 5 of differentiation) and Caco-2 monolayers at day 21, cultured as described in the cell culture section. All experiments were conducted in 96-well plates. Starting solutions were prepared in hCDM vehicle control or in Caco-2 vehicle control, both containing 0.5% DMSO.

Monolayers were initially washed twice with prewarmed HBSS (containing Ca^{2+} and Mg^{2+}) supplemented with 10 mM HEPES (pH 7.4) on both apical and basolateral sides, and 150 µL of NSAID (celecoxib or sulindac) starting solution was added to the apical compartment, with a range of concentrations tested as detailed in *Supplementary Table 7* (Appendix B.1, Table S7). Incubation periods of 2, 6, and 24h were assessed to evaluate drug accumulation.

After each specified incubation time, monolayers were washed twice with ice-cold HBSS containing 10 mM HEPES (pH 7.4). Intracellular compounds were extracted by incubating the cells for 1h at room temperature on an orbital shaker (250 rpm) with 150 µL cell lysis buffer (0.2 mg/mL BHT/EDTA in MeOH/water; 1:1 v/v). Lysates were diluted 1:1 with DMSO and stored at -80 °C until analysis. Cell diameter and live cell concentration were measured using the Cellometer® K2 Fluorescent Cell Counter (Nexcelom Bioscience), adhering to the manufacturer's guidelines. Protein content was quantified using the BCA method. These parameters were determined in representative wells to calculate the cellular volume (V_{cell}), assuming a spherical shape. A value of 6.5 µL/mg protein was retrieved from prior research (Mateus et al., 2013; Treyer et al., 2019, 2018), which closely aligned with our in-house estimations for Caco-2 monolayers, yielding a comparable V_{cell}.

Samples were analyzed using LC–MS/MS (Sections 2.3.3 to 2.3.6.) to quantify 127 eicosanoids (including PGs) at baseline and after treatment with increasing concentrations of celecoxib and sulindac. Baseline abundance was evaluated in both DMSO-free medium (vehicle controls) and DMSO-treated (0.5%) vehicle controls. The complete eicosanoid panel is presented in Table S2. Abundance levels were normalized to total protein and reported as ng eicosanoid/mg protein. Heatmaps illustrating baseline and post-treatment abundance levels were generated to aid visual interpretation of the results.

2.7. Data analysis

Data analysis was performed using Microsoft® Excel (Redmond, WA, USA) and results were visualized using GraphPad Prism 10.1.2 software (San Diego, CA, USA).

2.7.1. Apparent permeability coefficient (P_{app}) and efflux ratio (ER)

Transport across hCDMs or Caco-2 monolayers is expressed as a flux (dpm/s or ng/s). P_{app} was calculated from the slope of the transport time profile, divided by the surface area of the insert (0.143 cm^2 for hCDMs and 0.11 cm^2 for Caco-2) and the initial measured concentration in the donor compartment. P_{app} for each compound was determined using Eq. (1):

$$P_{app} = \frac{1}{A \times C_{t0}} + \frac{V_R \times \Delta C_R}{\Delta t} \quad (1)$$

where P_{app} is the permeability coefficient (x10^{-6} cm/s) in either the apical-to-basolateral (AP→BL) or in basolateral-to-apical (BL→AP) direction; A is the area of the filter (cm^2); C_{t0} is the concentration of the respective starting solution (dpm/mL or ng/mL); V_R is the volume of the receiver compartment (mL); and $\Delta C_R/\Delta t$ represents the change in substance concentration over time in the receiver compartment (dpm/mL or ng/mL x s). The transport rate was derived from the linear portion of the test (or reference) compound concentration versus time curve in the receiver compartment.

Efflux ratio (ER), determined from bidirectional studies, was calculated as the ratio of the secretory permeability, P_{app} [BL→AP], to the absorptive permeability, P_{app} [AP→BL], according to Eq. (2):

$$ER = \frac{P_{app\ [BL \rightarrow AP]}}{P_{app\ [AP \rightarrow BL]}} \quad (2)$$

ER ≥ 2 suggests that the test drug is a substrate for an efflux transporter (Hubatsch et al., 2007).

2.7.2. Unbound drug fraction in the cell ($f_{u,cell}$) and unbound intracellular drug concentration ($C_{u,cell}$)

The unbound drug fraction in the cell homogenate ($f_{u,hom}$) was determined employing Eq. (3):

$$f_{u,hom} = \frac{C_R}{C_D} \quad (3)$$

where C_R and C_D represent the compound concentrations in the receiver (buffer) and donor (homogenate) chambers of the RED device post-dialysis, respectively.

The unbound drug fraction in the cell ($f_{u,cell}$) was calculated by correcting for homogenate dilution (D) utilizing Eq. (4):

$$f_{u,cell} = \frac{1}{D \bullet \left(1 / f_{u,hom} - 1\right) + 1} \quad (4)$$

where D, derived using Eq. (5), was estimated to be 14 for a 20 x 10^6 cells/mL suspension of Caco-2 cells, based on a measured protein concentration in the cell homogenate (P_{hom}) of 11 mg/mL and a cellular volume (V_{cell}) of 6.5 µL/mg protein (Mateus et al., 2013; Treyer et al., 2019, 2018).

$$D = \frac{1}{P_{hom} \times V_{cell}} \quad (5)$$

The $f_{u,cell}$ values obtained in Caco-2 cells were deemed comparable in hCDMs and thus used as a surrogate for $f_{u,cell}$ in hCDMs without scaling factors, supported by evidence that $f_{u,cell}$ remains relatively conserved across different tissues and cell lines (Ryu et al., 2020; Treyer et al., 2019).

The unbound intracellular drug concentration ($C_{u,cell}$), representing the concentration available for binding to intracellular targets, was calculated by adjusting the total cellular concentration (C_{cell}) with $f_{u,cell}$, as indicated in Eq. (6):

$$C_{u,cell} = C_{cell} \times f_{u,cell} \quad (6)$$

2.7.3. Normalized viability and IC_{20}

The luminescent data for each condition was normalized to the corresponding DMSO-treated (0.5%) vehicle control to calculate normalized viability (% control), as specified in Eq. (7):

$$\textbf{normalized viability}\ (\%\ \textbf{control}) = \frac{\textbf{test compound viability}}{\textbf{DMSO viability}} \times 100 \quad (7)$$

Normalized viability (% control) was averaged at each concentration and the mean values were fitted to a 4-parameter logistic (4PL) nonlinear regression model, with the bottom set to 0, the top set to 100, and the Hill coefficient (nH) left unconstrained, to estimate the IC_{20} for each test compound in hCDMs and Caco-2 monolayers.

2.8. Statistical analysis

Statistical analyses were conducted using GraphPad Prism 10.1.2 software (San Diego, CA, USA). Data are presented as mean ± standard deviation (SD). To assess statistical differences among more than two groups, the Kruskal-Wallis nonparametric test (*H*-test) was applied, followed by Dunn's multiple comparisons test, for non-normally distributed data. The significance level (α) was set at 0.05, with a 95%

confidence interval (CI). Statistical significance was evaluated based on *p*-value, *P* (*ns* – not significant, $*P \leq 0.05$, $**P \leq 0.01$, $***P \leq 0.001$, $****P \leq 0.0001$). Asterisks (*) denote significant differences. Specific statistical tests used to infer differences between groups, along with the number of technical replicates, are outlined in the corresponding figure legends where applicable.

3. Results and discussion

3.1. Application of differentiated hCDMs in toxicity, cellular accumulation, and PD studies

To accelerate the adoption of new approach methodologies (NAMs) in industry—including CIVMs such as organoids and organs-on-chip—over preclinical animal studies or immortalized cell lines, it is imperative to establish robust context-of-use assays (Homan, 2023). To this end, we adapted a human colonoid-derived monolayer system as a physiologically relevant model of the human colon to investigate toxicity, cellular accumulation, and PD, as detailed in Sections 2.2.1–2.2.3.

Human adult stem cell-derived colonoids were established from cryopreserved healthy ascending colon epithelium of a single donor (Fig. 1*a*). Following 3D expansion, colonoids were dissociated and seeded as single cells onto microporous 96-well *Transwell*® inserts to form hCDMs. These proliferative monolayers were cultured in IntestiCult™ OGM for 11 days (Fig. 1*a*; 2D expansion, grey gradient), then differentiated in IntestiCult™ ODM for up to 5 days (Fig. 1*a*; 2D differentiation, light yellow gradient). The 96-well format enhanced throughput, facilitating dose-response, PD, and accumulation experiments, all benchmarked against Caco-2 monolayers (not depicted in the schematic).

Barrier integrity was assessed by measuring TEER (Fig. 1*b*), enabling non-invasive, longitudinal monitoring on the same transwells during expansion and differentiation. Confluence, defined as TEER $\geq 100\ \Omega \times cm^2$ (Jelinsky et al., 2023; Kourula et al., 2023; Parente et al., 2024), was reached between days 9–11, averaging $137.5 \pm 29.43\ \Omega \times cm^2$ ($n = 268$) by day 11. Switching to differentiation medium led to a progressive

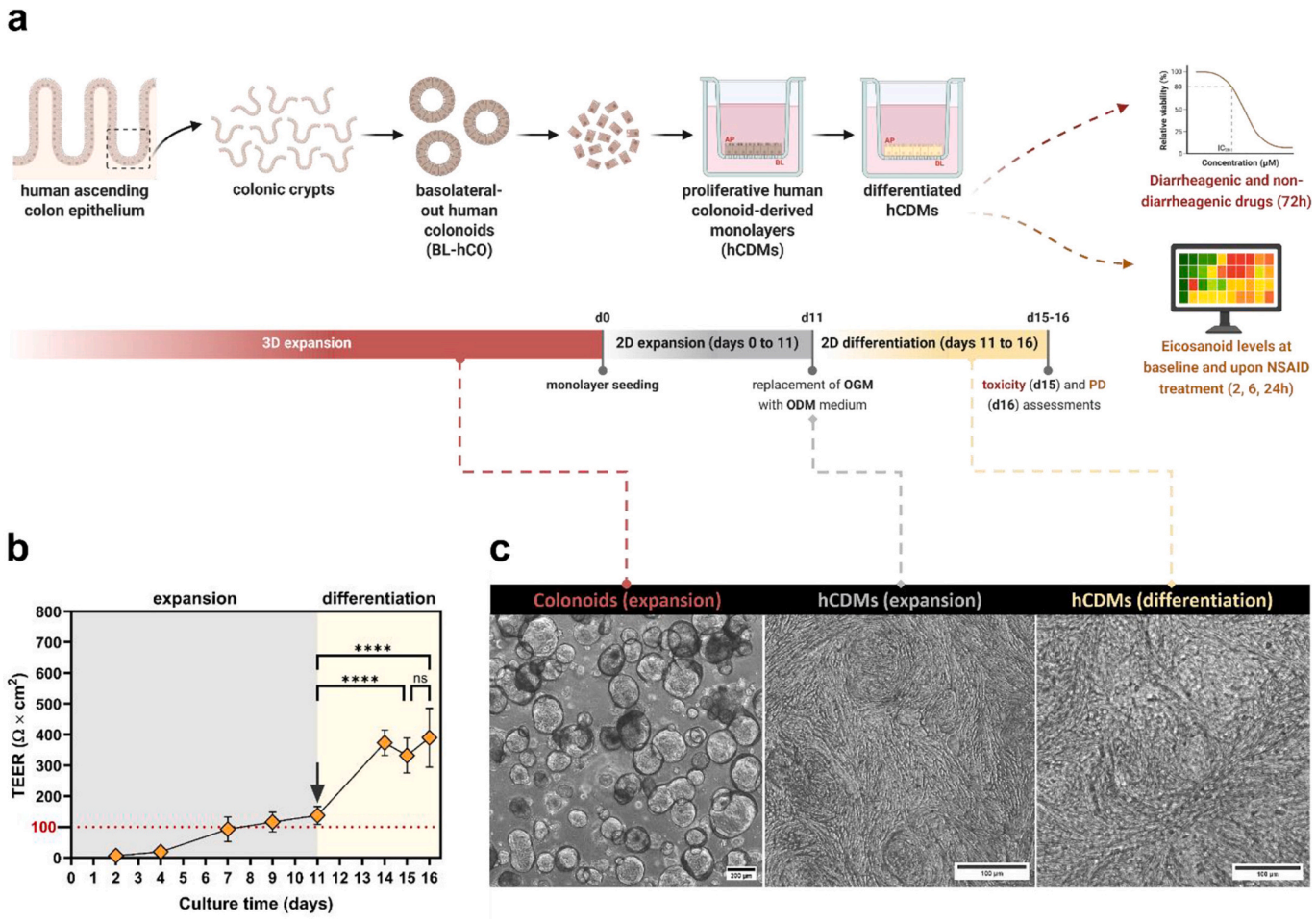

Fig. 1. Experimental setup and workflow for generating differentiated hCDMs. (a) Schematic of 2D hCDM generation. Proliferative, basolateral-out human 3D colonoids (BL-hCO) were derived from a cryopreserved stock of healthy human ascending colon epithelial tissue. After 3D expansion (dark red gradient), BL-hCO were dissociated into single cells and seeded onto microporous 96-well *Transwell*® inserts to form hCDMs. These underwent an initial expansion phase (days 0-11; grey gradient) followed by differentiation (days 11-16; light yellow gradient). Toxicity (red dashed arrow, *right*; day 15, day 4 of differentiation) and pharmacodynamic (PD) evaluations (orange dashed arrow, *right*; day 16, day 5 of differentiation) were conducted at differentiation endpoints. **(b) TEER measurements over an expansion and diferentiation time course.** TEER values for hCDMs were monitored over 16 days and recorded on days 2, 4, 7, 9, 11, 14, 15, and 16 ($n = 118–297$; orange rhombuses). Data represent mean ± SD. Statistics were performed using the Kruskal-Wallis test followed by Dunn's multiple comparisons test (*ns* – not significant, $****P \leq 0.0001$). The dotted red line at $100\ \Omega \times cm^2$ denotes the differentiation threshold, marking the transition from expansion (grey box) to differentiation (light yellow box) medium, with the downward black arrow at day 11 indicating the start of differentiation. **(c) Timeline representative brightfield images of colonoids and hCDMs.** *Left* (dark red): BL-hCO in expansion medium at day 14 of 3D culture (5 days post-split), ×4 magnification; *middle* (grey): hCDMs in expansion medium at day 11 of 2D culture (start of differentiation), ×20 magnification; *right* (light yellow): hCDMs in differentiation medium at day 14 of 2D culture (day 3 of differentiation), ×20 magnification. Scale bars: *left* (colonoids), black, 200 µm; *middle* and *right* (hCDMs), dark grey, 100 µm. Colors are consistent throughout (a-c): dark red (3D expansion), grey (2D expansion), and light yellow (2D differentiation).

increase in TEER during the first 3 days of differentiation (days 11–14) before plateauing from days 14–16.

Differentiated hCDMs exhibited average TEER values of 332.1 ± 52.02 Ω × cm^2 ($n = 166$) on day 15 and 390.4 ± 95.10 Ω × cm^2 ($n = 118$) on day 16 (Fig. 1*b*; day 15 vs. day 16, $P > 0.05$, *ns*). Noteworthy, these values, which were significantly higher than those measured at the onset of differentiation on day 11 (Fig. 1*b*; ****$P \leq 0.0001$), align with *ex vivo* human colon tissue reports (300–400 Ω × cm^2) and are markedly higher than those of the SI (12–120 Ω × cm^2) (Srinivasan et al., 2015).

TEER variability among human intestinal organoid-derived monolayers has been extensively reported. Interestingly, SI models sometimes exhibit paradoxically higher TEER than colonic models, contradicting *ex vivo* findings from human Ussing chambers (Parente et al., 2024). For instance, Kourula et al. observed TEER values of 1500 to 2000 Ω x cm^2 for differentiated human duodenal enteroid-derived monolayers cultured in enterocyte colon differentiation medium (eCDM) (Kourula et al., 2023), though literature values span from 209 to 2000 Ω x cm^2, with some studies reporting as low as 209 Ω x cm^2 for human ascending colonoid-derived monolayers (Nickerson et al., 2021). Similarly, human ileal enteroid-derived monolayers show variation ranging from 350 (Wright et al., 2023) to 1010 Ω x cm^2 (Nickerson et al., 2021). Such variability likely stems from donor-specific differences (Mohammadi et al., 2021), tissue source (e.g., different intestinal regions), and culture conditions (e.g., extracellular matrix composition, differentiation medium formulation, and duration of differentiation) (Tanaka et al., 2025; Yamashita et al., 2021).

Observations also suggest that human ileal- and colon organoid-derived monolayers exhibit lower TEER values than those derived from the proximal SI (Mohammadi et al., 2021; Nickerson et al., 2021; Wright et al., 2023). This observation is inconsistent with the known physiology of the intestinal barrier, as the colonic mucosa is inherently tighter than that of the SI (Lechuga et al., 2023). Furthermore, exceedingly high TEER values (around 2000 Ω x cm^2) are likely non-physiological, undermining the relevance of these organoid models for accurately modeling human barrier function (Srinivasan et al., 2015).

Brightfield microscopy (Fig. 1*c*) revealed that 3D colonoids in expansion medium had a cyst-like morphology with a large, central open lumen and typical basolateral-out polarity (Fig. 1*c*, left) (Sato et al., 2011). While brightfield imaging allows morphological inference, definitive confirmation of polarity would require immunostaining and confocal microscopy. Immunostaining for tight junction (e.g., ZO-1) or adherens junction (e.g., E-cadherin) markers was not performed in this study, as this characterization has previously been conducted in monolayers established from other donors (data not shown) and is well documented for intestinal organoid-derived monolayers (Tanaka et al., 2025; Yamashita et al., 2021).

By day 11, proliferative hCDMs reached confluence (Fig. 1*c*, middle). After 3 days in differentiation medium (day 14), monolayers became more compact and adopted a structured, epithelial-like architecture, accompanied by a marked TEER increase, suggesting the formation of functional tight junctions (Fig. 1*c*, right). Collectively, these results confirm that the differentiated hCDM system forms a polarized monolayer with colon-like barrier properties.

3.2. *Differentiated hCDMs as an in vitro tool to predict drug-induced diarrhea*

Intestinal AEs rank among the most prevalent clinical side effects, yet only a few *in vitro* models have been explored for routine screening (Belair et al., 2020; Federer et al., 2016; Klein et al., 2025; Peters et al., 2019; Pike et al., 2025). This contrasts with the ubiquitous use of intestinal epithelial cell lines (e.g., Caco-2) for drug absorption studies (Hubatsch et al., 2007; Sun et al., 2008).

Our previous research showed that differentiation media protocols can yield enterocyte-enriched human duodenal enteroid-derived monolayers that express markers of mature cell lineages, alongside metabolic activity and functional efflux transporters. Furthermore, we employed human 3D duodenal and colonic organoids to investigate drug-induced diarrhea, evaluating both diarrheagenic and non-diarrheagenic drugs using an ATP-based assay (Kourula et al., 2023).

To compare the cytotoxic responses of differentiated hCDMs and Caco-2 monolayers (Fig. 2 and Table 2), both models were incubated with six marketed small molecules (seven conditions total) in 0.5% DMSO (Fig. 2*b–h*), selected per criteria in Section 2.4. and summarized in Table 1, or with a 0.5% DMSO vehicle control for 72h prior to measuring ATP levels as an indicator of cell viability.

Prior studies with gefitinib applied to human duodenal enteroid-derived monolayers—exposed from the apical side only (drug uptake from the lumen, simulating the oral route), the basolateral side only (drug uptake from blood stream, mimicking IV route), or both—showed that toxicity was not observed when the compound was applied solely via the apical route (Kourula et al., 2023). Hence, for toxicity assessments, both surfaces were challenged to maximize compound exposure (Fig. 2*a*).

Exposure to erlotinib (Fig. 2*b*) and gefitinib (Fig. 2*c*), first generation EGFR-TKIs used to treat non-small cell lung cancer (NSCLC) and, in the case of erlotinib, advanced pancreatic cancer (Honeywell et al., 2020; Xu and Li, 2019), led to marked decreases in monolayer viability in differentiated hCDMs at day 15 (4 days in differentiation medium) and in Caco-2 monolayers at day 21, albeit to a lesser extent. Both compounds are diarrheagenic, with incidences of 54% and 29%, respectively (Table 2, diarrheagenic classification, "DC"). In hCDMs, erlotinib and gefitinib displayed IC_{20} values of 3.06 and 7.88 μM, respectively, compared to 36.84 and 21.42 μM in Caco-2 monolayers (Table 2). This results in erlotinib and gefitinib having IC_{20} values that are 12-fold and 3-fold lower in hCDMs than in the Caco-2 system. Analysis based exclusively on IC_{20} data suggests that hCDMs offer enhanced sensitivity to these drugs (Fig. 2*b* and 2*c*).

Other research employing CIVMs of the SI or colon (proliferative and differentiated) exposed to various EGFR-TKIs (Klein et al., 2025; Pike et al., 2024) underscores the necessity of considering the differentiation state of cells, as it can influence dose-response outcomes in toxicity testing. EGFR-TKIs inhibit tumor proliferation and induce apoptosis by blocking tyrosine kinase activity (Shah and Lester, 2020). Recent findings indicated that sorafenib, with a 43% diarrhea incidence, caused comparable viability decreases in both proliferative (grown in IntestiCult™ OGM) and differentiated (grown in IntestiCult™ ODM) human 3D duodenal organoids, with IC_{50} values of 10.03 μM and 8.42 μM, respectively (Klein et al., 2025). While EGFR-TKIs primarily target proliferative cells, the organoid differentiation state did not significantly alter predictions of sorafenib toxicity. Conversely, for afatinib, associated with a 96% diarrhea incidence, proliferative organoids were mostly affected as expected (IC_{50} of 0.036 μM), revealing a 100-fold lower IC_{50} than differentiated organoids (Klein et al., 2025). Supporting this, Pike and colleagues found that afatinib reduced the number of proliferating epithelial cells with negligible impact on differentiated epithelium in RepliGut® Planar, a human transverse colon-derived monolayer model (Pike et al., 2024).

We further evaluated two highly diarrheagenic antineoplastic agents: irinotecan (Fig. 2*d*) and its active metabolite, SN-38 (Fig. 2*f*). In both differentiated hCDMs and Caco-2 monolayers, irinotecan displayed an IC_{20} exceeding the highest concentration tested (>>110 μM; Table 2), indicating a lack of susceptibility to irinotecan-induced toxicity (Fig. 2*d*), which may be attributed to irinotecan being a MDR1/P-gp substrate (Parvez et al., 2021) (Table 1). The active efflux of irinotecan by P-gp results in insufficient intracellular levels to elicit a toxicity response. However, when this efflux was inhibited by elacridar (Fig. 2*e*), irinotecan showed an IC_{20} of 72.06 μM in differentiated hCDMs, indicating an increase in irinotecan's cytotoxicity likely due to elevation of its intracellular concentration (Xu and Villalona-Calero, 2002).

SN-38 exhibited an IC_{20} of 35.03 μM in hCDMs, whereas this value was about 4 times lower (7.98 μM) in the Caco-2 system (Table 2).

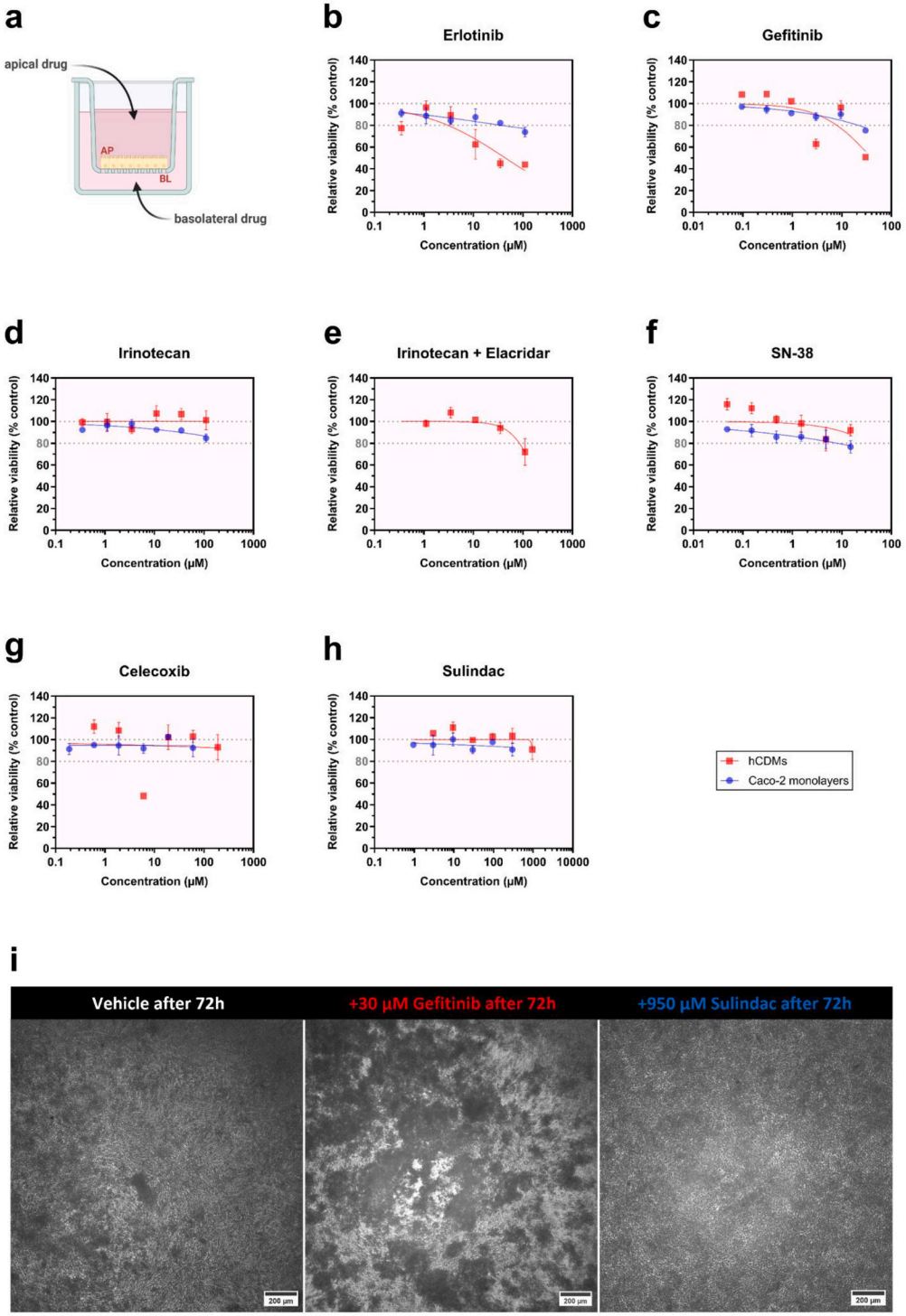

Fig. 2. Toxicity assessment of 6 marketed small molecules exhibiting varying clinical diarrhea incidence with differentiated hCDMs and Caco-2 monolayers. (a) Schematic of drug exposure in toxicity assays. Differentiated hCDMs and Caco-2 monolayers, grown in 96-well *Transwell*® inserts, were challenged with at least 5 concentrations of small molecules classified by their diarrheagenic potential (refer to "Reported Tox" in Table 1 and "Diarrheagenic Classification, DC" in Table 2 for details). Both apical (AP, top) and basolateral (BL, bottom) surfaces were treated to ensure maximal exposure. hCDMs were utilized at day 15 (day 4 of differentiation), and Caco-2 monolayers at day 21. **(b-h) Dose-response characterization.** Data represent mean ± S.D. of three technical replicates ($n = 3$) of relative viability normalized to the DMSO-treated (0.5%) vehicle control. Viability of differentiated hCDMs (red squares) and Caco-2 monolayers (blue circles) was determined by measuring cellular ATP levels with the CellTiter-Glo® 2.0 assay after 72h of exposure to: (b-f) diarrheagenic (erlotinib, gefitinib, irinotecan, and SN-38) and (g,h) non-diarrheagenic (celecoxib and sulindac) drugs at increasing concentrations (see Table S6). The small molecules tested include: (b) erlotinib, (c) gefitinib, (d) irinotecan, (e) irinotecan + elacridar, (g) SN-38, (g) celecoxib, and (h) sulindac. Dotted grey lines mark 80% and 100% relative viability, with dose-response curves fitted using a 4PL nonlinear regression model. **(i) Brightfield images.** Representative images of hCDMs at day 18 (day 7 of differentiation) following the 72-hour drug treatment, at ×4 magnification for: (*left*) DMSO-treated (0.5%) vehicle, (*middle*) 30 μM gefitinib (top dose), and (*right*) 950 μM sulindac (top dose). Scale bars, 200 μm. Color code: red (diarrheagenic), blue (non-diarrheagenic).

Table 2
Summary of diarrheagenic classification (DC), assay classification (AC), classification outcome (CO), fraction unbound in plasma ($f_{u,p}$), clinical maximum plasma concentration (C_{max}), unbound C_{max} ($C_{max,u}$), concentration required for 20% inhibition (IC_{20}), and unbound IC_{20} ($IC_{20,u}$) for intestinal test small molecules determined in toxicity assays using hCDMs and Caco-2 monolayers. COs were established using a threshold set at 30×C_{max}.

Compound	DC[a]	AC[b]	CO[c]	$f_{u,p}$[d]	C_{max}[e] (total, μM)	$C_{max,u}$ (unbound, μM)	IC_{20} (total, μM)	$IC_{20,u}$[f] (unbound, μM)	$IC_{20}/30\times C_{max}$[b,c]	$IC_{20,u}/C_{max,u}$
					hCDMs					
Erlotinib*	+	+	TP	0.070	3.53	0.247	3.06	0.07	0.03	0.28
Gefitinib*	+	+	TP	0.089	1.00	0.089	7.88	0.04	0.26	0.48
Irinotecan*	+	−	FN	0.199	3.19	0.634	>>110[§,†]	*n.d.*	>>1.15	*n.d.*
Irinotecan + Elacridar	+	+	TP	0.199	3.19	0.634	72.06	*n.d.*	0.75	*n.d.*
SN-38*	+	−	FN	0.021	0.38	0.008	35.03	*n.d.*	3.06	*n.d.*
Celecoxib*	−	−	TN	0.002	1.84	0.004	>>60[§]	>>0.13	>>1.09	>>32.70
Sulindac*	−	−	TN	0.060	9.37	0.562	>>300[§]	>>51.96	>>1.07	>>92.41
					Caco-2 monolayers					
Erlotinib*	+	+	TP	0.070	3.53	0.247	36.84	0.83	0.35	3.35
Erlotinib + Elacridar	+	+	TP	0.070	3.53	0.247	43.87	0.99	0.41	3.99
Gefitinib*	+	+	TP	0.089	1.00	0.089	21.42	0.12	0.71	1.30
Gefitinib + Elacridar	+	+	TP	0.089	1.00	0.089	20.08	0.11	0.67	1.22
Irinotecan*	+	−	FN	0.199	3.19	0.634	>>110[§,†]	*n.d.*	>>1.15	*n.d.*
SN-38*	+	+	TP	0.021	0.38	0.008	7.98	*n.d.*	0.70	*n.d.*
Celecoxib*	−	−	TN	0.002	1.84	0.004	>>60[§]	>>0.13	>>1.09	>>32.70
Sulindac*	−	−	TN	0.060	9.37	0.562	>>300[§]	>>51.96	>>1.07	>>92.41

[a] Binary classification, where positive [+] indicates a clinical diarrhea incidence >25% and/or a black box warning for intestinal side effects, and negative [−] denotes a diarrhea incidence of 0-5%. Diarrhea incidence by drug: Erlotinib – 54% (TARCEVA®, Prescribing Information, 2010); Gefitinib – 29% (IRESSA®, Prescribing Information, 2018); Irinotecan and SN-38 – 85% and black box warning for diarrhea (CAMPTOSAR®, Prescribing Information, 2014); Celecoxib – <5% (CELEBREX®, Prescribing Information, 2008); Sulindac – 3-9% (CLINORIL®, Prescribing Information, 2010).

[b] Compounds with $IC_{20}/30\times C_{max} < 1$ were classified as assay positives [+], according to Belair et al. (2020), Lin and Will (2012), Kourula et al. (2023) and Klein et al. (2025).

[c] COs were scored using $IC_{20}/30\times C_{max} < 1$ as diarrheagenic criterion: FN (false negative), TN (true negative), TP (true positive).

[d] Erlotinib and gefitinib: $f_{u,p}$ sourced from Lombardo et al. (2018); irinotecan and SN-38: $f_{u,p}$ retrieved from Combes et al. (2000); celecoxib and sulindac: $f_{u,p}$ generated internally.

[e] C_{max} were sourced as follows: erlotinib from Prados et al. (2006), gefitinib from Hirose et al. (2016), irinotecan from Denlinger et al. (2009), SN-38 from Chabot et al. (1995), celecoxib from CELEBREX®, Clinical Pharmacology/Biopharmaceutics Review (1998), and sulindac from Reid et al. (2008). These values were obtained after the first doses of 100 mg QD for erlotinib, 250 mg QD for gefitinib, 180 mg/m^2 for irinotecan (FOLFIRI regimen), 600 mg/m^2 of irinotecan q3wk for SN-38, 200 mg QD for celecoxib, and 150 mg as a single dose for sulindac. OD – Once daily, and q3wk – Once every three weeks.

[f] $IC_{20,u}$ was derived by multiplying IC_{20} by the corresponding unbound drug fraction in the cell ($f_{u,cell}$). $IC_{20,u}$ values for irinotecan and SN-38 were not calculated as $f_{u,cell}$ for these compounds was not determined (*n.d.*). $f_{u,cell}$ values for celecoxib and sulindac are presented in Table 3, while those for erlotinib and gefitinib can be found in Table S9.

[§] Values are reported as exceeding the highest concentration tested (i.e., >> the highest concentration). In these instances, the observed effect did not reach the IC_{20} level, indicating that viability remained above 80% at the highest concentration.

[†] Viability was 100.92 ± 7.15% for hCDMs and 84.67 ± 3.14% for Caco-2 monolayers at a 110 μM irinotecan treatment.

[*] Asterisks indicate the common conditions assessed in hCDMs and Caco-2 monolayers.

Interestingly, this is the only instance where a diarrheagenic compound had a lower IC_{20} in Caco-2 monolayers versus hCDMs. The efficacy and safety profile of irinotecan is closely tied to its hydrolysis to SN-38 by CES2 in enterocytes, followed by the conversion of SN-38 to its inactive form, SN-38-G, via glucuronidation by UGT1A1 (Parvez et al., 2021; Teft et al., 2015) (Table 1). Former investigations showed that UGT1A1 activity in human colonic organoids is roughly 5-fold higher than in duodenal organoids (Kourula et al., 2023). In contrast, Caco-2 monolayers express low levels of all UGTs except UGT1A6, although expression levels rise with differentiation (Siissalo et al., 2008). Thus, in our hCDM system, it is plausible that SN-38 was rapidly converted to non-toxic SN-38-G by UGT1A1. Further studies are warranted, as SN-38-G was not quantified in this investigation.

In addition to irinotecan, erlotinib and gefitinib are known MDR1/P-gp and BCRP substrates (Honeywell et al., 2020) (Table 1). Co-administration with elacridar in Caco-2 monolayers did not

significantly change IC_{20}: erlotinib ranged from 36.84 to 43.87 μM, while gefitinib from 21.42 to 20.08 μM (Table 2). We performed bidirectional transport studies with erlotinib and gefitinib in the presence and absence of elacridar in Caco-2 monolayers, calculating the ERs for each condition (Table S8). Noteworthy, the absorptive transport of both drugs exceeded their secretory transport, resulting in ER < 2.0, suggesting neither acts as a substrate for P-gp and BCRP in Caco-2 monolayers, potentially explaining the minimal IC_{20} differences observed with and without elacridar. Since both EGFR-TKIs were tested at 10 μM to resemble the *in vivo* scenario of high intraluminal drug gut concentrations (Peters et al., 2020), we stress that the experimental design was not tailored to perform drug efflux transporter studies. Using 10 μM may have led to transporter saturation; follow-up studies at a lower donor concentration would be needed to confirm this hypothesis.

Celecoxib (Fig. 2*g*) and sulindac (Fig. 2*h*), both NSAIDs, are non-diarrheagenic, with clinical diarrhea incidences below 5% (Table 2). Despite this, NSAIDs can induce intestinal mucosal damage in both normal enterocytes and colon cancer cells, although the underlying MoT remains poorly understood (Fornai et al., 2014; Thun et al., 2002). Consistent with their low diarrhea incidences, neither drug affected monolayer viability across the tested concentration range in either model. In fact, their IC_{20} values exceeded the highest concentrations assessed (>>60 μM for celecoxib and >>300 μM for sulindac; Table 2) in both differentiated hCDMs and Caco-2 monolayers, reinforcing their non-diarrheagenic classification. Klein et al. also noted minimal viability decreases at 100 μM for acetylsalicylic acid, another NSAID, in differentiated versus proliferative human 3D duodenal organoids, with an IC_{50} of 626 μM in differentiated organoids (Klein et al., 2025), surpassing the maximum concentrations tested in our experiments for celecoxib and sulindac.

The organization and morphology of hCDMs following drug exposure were monitored using brightfield microscopy (Fig. 2*i*). After 72h (day 18; 7 days in differentiation medium), micrographs revealed intact epithelial architecture in the DMSO-treated vehicle (Fig. 2*i*, left). In contrast, 30 μM gefitinib induced loss of confluence and numerous detached cell clumps, resulting in a frayed, uneven appearance (Fig. 2*i*, middle). Conversely, 950 μM sulindac did not elicit any detectable structural changes (Fig. 2*i*, right). These observations concurred with the ATP-based viability data, further validating our findings.

3.3. Small molecules with heterogeneous clinical diarrhea incidence elicit differential toxicity in differentiated hCDMs and Caco-2 monolayers

Efforts to harmonize *in vitro* screening for drug-induced diarrhea have shown that the IC_{15} to 80× human C_{max} ratio optimally differentiates diarrheagenic from non-diarrheagenic agents within a 31-drug panel, using TEER-based assays with EpiIntestinal™ microtissues (Peters et al., 2019). IC_{15} enabled quantification of compounds with <50% inhibition at the highest tested concentration (Peters et al., 2019; Pike et al., 2025), guiding our selection of IC_{20} over IC_{50} in this study, as detailed in Section 2.5.1. Extending this, Pike and colleagues applied the same margin to the 31-drug set with RepliGut® Planar, integrating cell quantification endpoints—5-ethynyl-2'-deoxyuridine (EdU) for proliferative cell abundance and 4′,6-diamidino-2-phenylindole (DAPI) for total cell count—alongside TEER measurements (Pike et al., 2024).

Lin and Will found that normalizing cytotoxicity predictions to 30× and 100× human C_{max} greatly improves predictivity over 1× C_{max} (Lin and Will, 2012). Their findings align with Belair et al., who showed that compounds with an IC_{50} below 30× C_{max} could be classified as diarrheagenic with 90% accuracy in human 3D ileal organoids cultured in IntestiCult™ OGM medium (Belair et al., 2020), using the previously tested drug set (Peters et al., 2019). Direct comparison indicated that 30× C_{max} offered higher sensitivity and specificity than 100× (Belair et al., 2020). Klein et al. also employed this threshold in studies with human 3D duodenal organoids, comparing proliferative organoids in IntestiCult™ OGM with differentiated cultures in IntestiCult™ ODM medium (Klein et al., 2025). Likewise, Kourula et al. adopted the 30× C_{max} normalization to assess proliferative human 3D duodenal and colonic organoids (Kourula et al., 2023).

To translate *in vitro* toxicity data to clinical outcomes, we adopted a conservative approach and calculated $IC_{20}/30\times C_{max}$ ratios, designating a drug as diarrheagenic (assay positive) if $IC_{20}/30\times C_{max} < 1$. This follows the established safety margin threshold of 30× C_{max} for organoids cultured in IntestiCult™ OGM (Belair et al., 2020; Klein et al., 2025) or ODM medium (Klein et al., 2025), where IC_{50} values were derived. Fig. 3 illustrates the $IC_{20}/30\times C_{max}$ ratios for all tested small molecules in differentiated hCDMs (Fig. 3*a*, left) and Caco-2 monolayers (Fig. 3*b*, right).

Evaluation of the six common conditions (asterisked in Fig. 3 and Table 2) revealed consistent classification across both hCDMs and Caco-2 monolayers, except for SN-38.

In the present study, both models correctly identified the EGFR-TKIs (erlotinib and gefitinib) as true positive (TP) and the NSAIDs (celecoxib and sulindac) as true negative (TN). Specifically, erlotinib and gefitinib (diarrheagenic) yielded $IC_{20}/30\times C_{max}$ of 0.03 and 0.26 in hCDMs, and 0.35 and 0.71 in Caco-2, underscoring the heightened sensitivity of hCDMs for these two TKIs. Inhibiting MDR1/P-gp and BCRP efflux with elacridar in Caco-2 monolayers did not meaningfully impact $IC_{20}/30\times C_{max}$ values (erlotinib: 0.35 to 0.41; gefitinib: 0.71 to 0.67), with both compounds retaining their TP categorization. Analysis of C_{cell} and $C_{u,cell}$ for these TKIs in Caco-2 monolayers (±elacridar; Table S9) confirmed that gefitinib reached higher total and unbound intracellular concentrations than erlotinib, which parallels erlotinib's higher cytotoxicity in our assays and its elevated clinical incidence of diarrhea (54%; Table 2). Importantly, elacridar treatment did not significantly affect C_{cell} or $C_{u,cell}$ for either TKI, mirroring the minimal changes seen in IC_{20} and $IC_{20}/30\times C_{max}$ ratios. Notably, celecoxib and sulindac (non-diarrheagenic) were accurately classified as assay negatives in both systems ($IC_{20}/30\times C_{max}$ >> 1.09 for celecoxib and >> 1.07 for sulindac), showing <20% inhibition at the highest concentrations tested.

In contrast, irinotecan—despite being diarrheagenic—was misclassified as a false negative (FN) in both models, with $IC_{20}/30\times C_{max}$ >> 1.15. This outcome reflects its status as a MDR1/P-gp substrate (Parvez et al., 2021), as noted earlier. Inhibition of P-gp-mediated efflux with elacridar lowered $IC_{20}/30\times C_{max}$ to 0.75, reclassifying it as a TP. This shift indicates that blocking active drug efflux enhanced its cytotoxicity, presumably owing to higher intracellular irinotecan concentration (Xu and Villalona-Calero, 2002).

SN-38 was correctly classified as diarrheagenic in the Caco-2 system ($IC_{20}/30\times C_{max}$ of 0.70; TP), but misclassified as non-diarrheagenic in hCDMs ($IC_{20}/30\times C_{max}$ of 3.06; FN), signaling reduced hCDM sensitivity to SN-38. This discrepancy likely arises from high UGT1A1 activity in human colonic organoids (Kourula et al., 2023), driving rapid conversion of SN-38 to its non-toxic glucuronide (SN-38-G), whereas UGT1A1 is underexpressed in Caco-2 monolayers (Siissalo et al., 2008). As such, efficient SN-38 detoxification in hCDMs may underlie the misclassification in the organoid-derived monolayer system.

The unbound fraction in plasma ($f_{u,p}$) for each drug defines the unbound C_{max} ($C_{max,u}$), while $f_{u,cell}$ can be used to estimate the free IC_{20} ($IC_{20,u}$). Incorporating these parameters into our calculations can refine $IC_{20}/30\times C_{max}$ estimates. We sourced $f_{u,p}$ from the literature (Table 2) and estimated $f_{u,cell}$ via equilibrium dialysis (Table 2, Table 3 and Table S9). The resulting unbound ratios, $IC_{20,u}/C_{max,u}$, were then determined.

Analysis of unbound ratios showed that erlotinib and gefitinib yielded values of 0.28 and 0.48 in hCDMs, versus 3.35 and 1.30 in Caco-2 monolayers. Celecoxib and sulindac exhibited considerably higher ratios (>>32.70 and >>92.41, respectively) across both models. Within hCDMs, $IC_{20,u}$ values for erlotinib and gefitinib are approximately 4-fold and 2-fold lower than their respective $C_{max,u}$, correctly classifying them as diarrheagenic ($IC_{20,u} < C_{max,u}$) and aligning their ranking with the reported diarrhea incidences. By contrast, in the Caco-2 system, $IC_{20,u}$

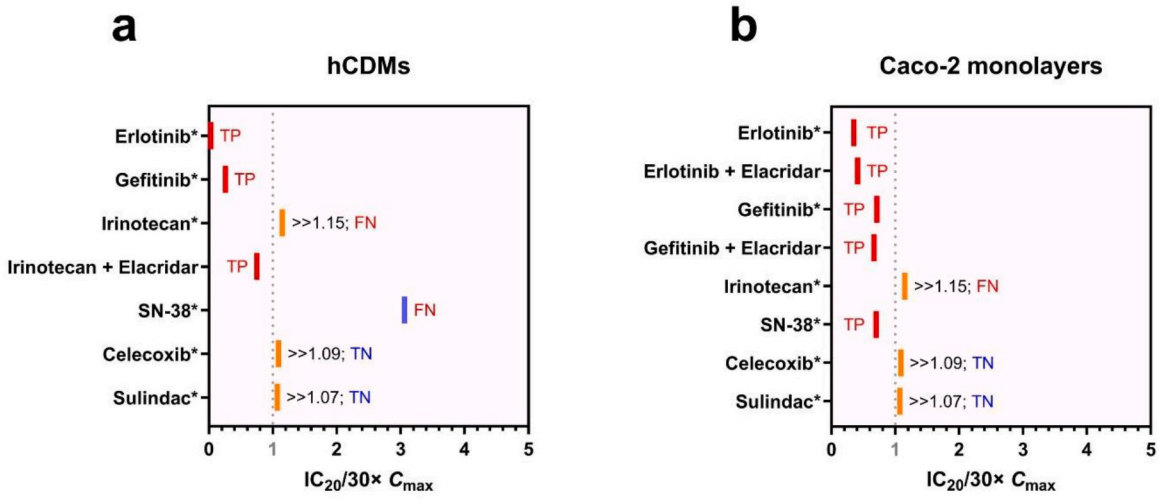

Fig. 3. 30×C_{max}–normalized IC_{20} toxicity predictions for the response of reference small molecules. Data represent the mean $IC_{20}/30\times C_{max}$ ratio for each drug, categorized as diarrheagenic (red) or non-diarrheagenic (blue) based on clinical diarrhea incidence referenced in Table 2 (see "Diarrheagenic Classification, DC"), shown for **(a)** hCDMs (*left*) and **(b)** Caco-2 monolayers (*right*). IC_{20} values were derived by curve fitting as depicted in Fig. 2. Key parameters—including DC, assay classification (AC), classification outcome (CO), IC_{20}, and $IC_{20}/30\times C_{max}$—are detailed in Table 2. Dotted grey lines mark the cutoff of $IC_{20}/30\times C_{max} < 1$, defining assay positives. Red bars signifiy assay positives, blue bars denote assay negatives, and orange bars indicate conditions where the observed effect did not reach the IC_{20} level, with values reported as exceeding the highest concentration tested (see footnote "§" in Table 2). COs were graded as follows: FN (false negative) for drugs exhibiting intestinal toxicity according to publicly available data but classified as assay-negative; TN (true negative) for drugs with no intestinal toxicity classified as assay-negative; and TP (true positive) for drugs with intestinal toxicity classified as assay-positive. Asterisks (*) highlight conditions evaluated in both hCDMs and Caco-2 monolayers.

for erlotinib and gefitinib surpass $C_{max,u}$ ($IC_{20,u} > C_{max,u}$), which would misclassify them as non-diarrheagenic. Moreover, in Caco-2 monolayers the unbound ratio for erlotinib is higher than that for gefitinib, which is inconsistent with their diarrhea incidences. NSAIDs remained non-diarrheagenic ($IC_{20,u} > C_{max,u}$) in both systems.

Defining a safety margin from our limited drug set warrants caution. Preliminary analysis suggests that a cutoff below $30\times C_{max,u}$ (e.g., 5 to $10\times C_{max,u}$) may suffice to effectively segregate diarrheagenic from non-diarrheagenic drugs, as the highest $IC_{20,u}/C_{max,u}$ observed was 3.99 (Erlotinib + Elacridar in Caco-2). Nonetheless, larger datasets and broader validation across different laboratories are needed to establish a robust safety margin based on unbound ratios. Future investigations with gut CIVMs to predict clinical intestinal toxicity would benefit from estimating free drug concentrations in the gut, allowing more meaningful comparisons of *in vitro* IC_{20} with the actual exposures required to elicit intestinal AEs.

Currently, total plasma C_{max} is the standard for normalizing *in vitro* potency values (e.g., effective or inhibitory concentrations), despite its variability with dose and administration route (Peters et al., 2020). Intraluminal colonic concentrations, estimated for all compounds (data

Table 3
Total cellular (C_{cell}) and unbound intracellular ($C_{u,cell}$) concentrations of the NSAIDs celecoxib and sulindac following increasing incubation periods and doses in hCDMs.

Compound	Concentration[a] (μM)	Sampling Timepoints (h)	C_{cell}[b] (total, μM)	$C_{u,cell}$[c] (unbound, μM)	$f_{u,cell}$[d*]
			hCDMs		
Celecoxib	19	2	160.46 ± 8.05	0.35 ± 0.02	0.0022 ± 0.0002
	[CXB 1]	6	245.67 ± 28.22	0.54 ± 0.06	
		24	163.42 ± 8.06	0.36 ± 0.02	
	60	2	520.99 ± 25.73	1.15 ± 0.06	
	[CXB 2]	6	727.33 ± 53.60	1.60 ± 0.12	
		24	638.41 ± 95.37	1.40 ± 0.21	
	190	2	1724.85 ± 81.39	3.79 ± 0.18	
	[CXB 3]	6	2063.43 ± 98.73	4.54 ± 0.22	
		24	2177.44 ± 182.85	4.79 ± 0.40	
Sulindac	95	2	38.43 ± 1.46	6.66 ± 0.25	0.1732 ± 0.0344
	[SL 1]	6	31.96 ± 2.29	5.54 ± 0.40	
		24	35.56 ± 2.70	6.16 ± 0.47	
	300	2	149.01 ± 11.27	25.81 ± 1.95	
	[SL 2]	6	79.47 ± 6.14	13.76 ± 1.06	
		24	113.26 ± 18.67	19.62 ± 3.23	
	950	2	611.15 ± 94.09	105.85 ± 16.30	
	[SL 3]	6	264.10 ± 67.51	45.74 ± 11.69	
		24	685.56 ± 53.61	118.74 ± 9.28	

[a] 1, 2, and 3 indicate the nominal concentrations of celecoxib (CXB) and sulindac (SL) during incubation, with the corresponding measured $C_{u,cell}$ values illustrated in Fig. 5*b*.

[b-d] C_{cell},$C_{u,cell}$, and $f_{u,cell}$ are reported as the mean ± S.D. of three replicates ($n = 3$).

[*] $f_{u,cell}$ was measured at a cell of density of 20 million cells/mL, 1 μM test compound concentration, and 6-hour incubation time in Caco-2 cells; these values were deemed comparable in hCDMs and used as a surrogate for $f_{u,cell}$ in hCDMs (Ryu et al., 2020; Treyer et al., 2019).

not shown) except intravenously administered irinotecan and SN-38, were several orders of magnitude higher than 30× C_{max} and are likely more physiologically relevant—particularly for oral drugs—yet are challenging to measure and highly uncertain (Peters et al., 2020; Tanaka et al., 2015). Colonic volume estimates vary widely depending on methodology (Lemmens et al., 2021; Schiller et al., 2005), and the presence of localized free water "pockets", especially in the ascending colon, further contributes to regional concentration differences (Murray et al., 2017). Due to these uncertainties, we used 30× C_{max} for IC_{20} normalization.

Several important pitfalls should be considered when working with differentiated 3D or 2D primary tissue-derived organoid models. A major constraint is the short lifespan of terminally differentiated cells, making the duration of differentiation a challenging factor (Zachos et al., 2016). In both rodents and humans, enterocytes and colonocytes have a lifespan of 5 to 7 days (Van Lieshout et al., 2004; Zachos et al., 2016). With this constraint in mind, we conducted toxicity evaluations with hCDMs starting on day 4 of differentiation and extending incubations through day 7 (after 72h) in differentiation medium. When monitoring TEER in DMSO-treated vehicle controls, the Caco-2 profile exhibited a flat line over 72h, whereas hCDMs showed a decline in TEER from 48 to 72h (day 6 to day 7 of differentiation); however, values stayed above the 100 Ω × cm^2 threshold (Fig. S1). Brightfield micrographs confirmed that hCDMs preserved intact epithelial architecture after 72h in the DMSO-treated vehicle (Fig. 2*i*, left). Taken together with ATP-based viability data (Fig. 2 and Table 2), these findings support the suitability of hCDMs for toxicity-based predictions within this differentiation window.

As some studies have linked diarrhea predictivity to intestinal barrier dysfunction assessed via TEER, we recorded the TEER responses of hCDMs and Caco-2 monolayers after exposure to our drug panel (Fig. S2). Caco-2 monolayers showed no discernible dose-response, irrespective of compound or timepoint, while hCDMs demonstrated a more pronounced dose-dependent reduction in TEER at 48 and 72h. Prior work with organotypic models suggests that TEER may be less sensitive to drug-induced toxicity than cell quantification endpoints such as EdU or DAPI (Pike et al., 2025). Additionally, TEER readings are prone to technical variability from pH, gas exchange, temperature, medium composition, and electrode positioning (Srinivasan et al., 2015), which contribute to noise and variance. Still, TEER offers valuable real-time insights into barrier integrity and overall epithelial cell monolayer health (Peters et al., 2019; Srinivasan et al., 2015). As IC_{20} values were not generated from TEER data, direct comparison with CellTiter-Glo®-based dose-response curves was not feasible. Future studies are needed for such a head-to-head analysis.

A difference adding translational relevance to colonoids over Caco-2 monolayers is the presence of goblet cells and a mucus layer, absent in Caco-2 under standard culture (Sun et al., 2008). Mitrofanova and team reported that colonoids from the same organoid line used here contain mucus-producing goblet cells ($MUC2^+$), with Alcian Blue and Periodic Acid-Schiff staining confirming a mucus layer resembling the *in vivo* state (Mitrofanova et al., 2024). In our previous work, we likewise showed Alcian $Blue^+$ staining and MUC2 gene expression in human colonoids, indicating *in vivo*-like architecture (Kourula et al., 2023). In the colon, secreted MUC2 and other components form a thick protective barrier; however, under *in vitro* conditions this barrier is unlikely to notably affect drug disposition or cytotoxicity (Mitrofanova et al., 2024). Mucus binding may slow diffusion and influence the disposition of lipophilic small molecules (Witten et al., 2019), but this remains to be investigated in organotypic models.

Although transporter expression and metabolic capacity were not examined here, irinotecan/SN-38 experiments illustrate how active efflux and metabolic processes can influence intracellular drug accumulation and toxicity. Inhibition of P-gp efflux increased cytotoxicity, whereas UGT1A1-mediated metabolism in hCDMs likely reduced toxic SN-38 levels via SN-38-G formation, underscoring the importance of incorporating these determinants in future studies to refine *in vitro* toxicity assessment.

Despite the limited size of our drug panel and the use of a single donor, our results mirror recent reports using 3D or 2D organoid-derived monolayer models (Belair et al., 2020; Klein et al., 2025; Kourula et al., 2023; Pike et al., 2025), supporting the utility of hCDM-based viability assays for capturing drug-induced intestinal toxicity.

3.4. *hCDMs provide a colon-like representation of the PG pathway, while Caco-2 monolayers portray cancer tissue abundance levels*

Although there are context-of-use applications for toxicity assessment utilizing SI and colonic CIVMs, PD investigations have not yet been extensively explored using these complex models, likely due to the multitude of mechanisms through which PD interactions can occur (O'Mahony et al., 2025).

We profiled the eicosanome of differentiated hCDMs on day 16 (5 days in differentiation medium) and Caco-2 monolayers, examining the abundance of 127 eicosanoids at baseline in DMSO-treated (0.5%) medium over 24h. A detailed list of the quantified analytes is presented in Table S2. Free AA, a precursor that converts into a range of prostanoids—including PGs and thromboxanes (TXs)—via the COX enzyme family (Wang et al., 2005), was selected for analysis alongside specific PGs: $PGF_{2\alpha}$, PGE_2+PGD_2, 15k $PGF_{2\alpha}$, 15k PGE_2, dhk $PGF_{2\alpha}$, dhk PGD_2, and dhk PGE_2. This selection is illustrated in Fig. 4 for both hCDMs (Fig. 4*a*, left) and Caco-2 monolayers (Fig. 4*b*, right). These PGs were chosen for their roles in a wide array of physiological and pathological processes within the GI tract (Wang et al., 2005).

At baseline, free AA was absent in both hCDMs and Caco-2 monolayers, as anticipated. In general, hCDMs demonstrated a time-dependent increase in PG abundance throughout the 24-hour duration (Fig. 4*a*), a trend not reflected in Caco-2 monolayers (Fig. 4*b*). Additionally, some significant PGs, such as 15k PGE_2, were not detected at baseline in the Caco-2 system.

Studies on PG production in human CRC have shown that colorectal tumor cells produce $PGF_{2\alpha}$, which plays a crucial role in colorectal tumorigenesis (Qualtrough et al., 2007). Furthermore, $PGF_{2\alpha}$ is secreted by both colorectal adenoma and carcinoma-derived cell lines at levels exceeding those of PGE_2 (Nugent et al., 1996; Qualtrough et al., 2007). Our findings demonstrate that Caco-2 monolayers display intrinsically higher abundance levels of $PGF_{2\alpha}$ and its oxidized metabolite, 15k $PGF_{2\alpha}$ (Fig. 4*b*), compared to hCDMs. This suggests that the elevated levels of $PGF_{2\alpha}$ (and 15k $PGF_{2\alpha}$) in Caco-2 monolayers may be attributed to their origin as an immortalized cell line derived from human colorectal adenocarcinoma.

The baseline signatures of a subset of PGs in the 0.5% DMSO-treated vehicles (Fig. 4) were compared to those in DMSO-free culture medium (Fig. S3). DMSO is known to be cytotoxic at concentrations of ≥5% of the total medium volume (Nguyen et al., 2025). OECD guidelines recommend DMSO concentrations of ≤0.5% for *in vitro* assays to minimize cytotoxic effects (Nguyen et al., 2025). As expected, results showed that 0.5% DMSO had no significant impact on PG abundance, prompting us to use these baseline conditions (Fig. 4) for comparison in subsequent evaluations.

Altogether, hCDMs provided a colon-like depiction of the PG pathway, while the Caco-2 model accurately reflected the pathophysiology associated with its cancerous tissue origin, as evidenced by the elevated levels of $PGF_{2\alpha}$ and 15k $PGF_{2\alpha}$.

3.5. *Celecoxib treatment lowers PG abundance in hCDMs in a concentration-dependent manner, an effect not discernible in the Caco-2 system*

NSAIDs are frequently prescribed to relieve acute pain and inflammation associated with conditions such as arthritis, migraines, and postoperative recovery. Their MoA involves the inhibition of COX

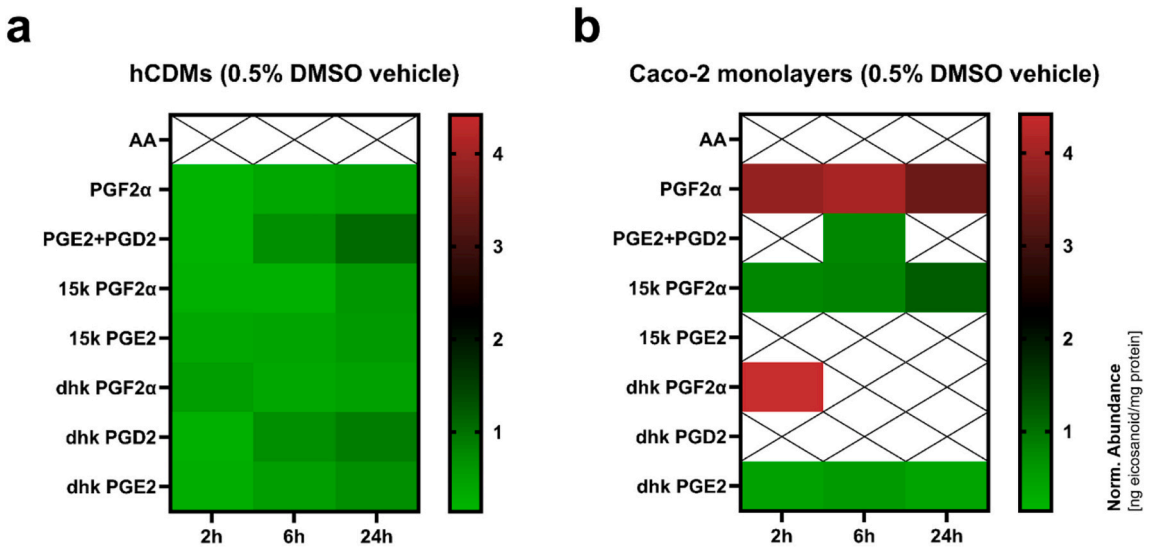

Fig. 4. Baseline signatures of selected eicosanoids. Heatmaps depict median baseline abundance levels in DMSO-treated (0.5%) medium for **(a)** hCDMs (*left*) and **(b)** Caco-2 monolayers (*right*). The displayed eicosanoids, listed from top to bottom, include arachidonic acid (AA), a precursor molecule, and its derived prostaglandins: prostaglandin F2α (PGF2α); prostaglandin E2 combined with prostaglandin D2 (PGE2+PGD2); 15-keto prostaglandin F2α (15k PGF2α); 15-keto prostaglandin E2 (15k PGE2); 13,14-dihydro-15-keto prostaglandin F2α (dhk PGF2α); 13,14-dihydro-15-keto prostaglandin D2 (dhk PGD2); and 13,14-dihydro-15-keto prostaglandin E2 (dhk PGE2). PD evaluations were conducted on hCDMs at day 16 (day 5 of differentiation) and on Caco-2 monolayers at day 21. Abundance levels, represented by green double gradients, were measured at 2, 6, and 24h, normalized to total protein content, and expressed in ng eicosanoid/mg protein, with darker shades indicating higher levels. Results reflect three technical replicates ($n = 3$). A cross symbol indicates abundance levels below the lower limit of quantification (LLOQ). The complete 127-eicosanoid panel, including each eicosanoid's LLOQ, is detailed in Table S2.

enzymes, which reduces the production of PGs that contribute to inflammation (Wirth et al., 2024).

Decades of research and clinical trials indicate that the use of NSAIDs and COX-2 selective inhibitors correlates with a decreased risk of certain malignancies, including human CRC (Wang et al., 2005). The first body of evidence establishing a positive relationship between COX-2 expression and human CRC was reported in 1994 by Eberhart and colleagues (Eberhart et al., 1994), with subsequent studies confirming elevated COX-2 expression in approximately 50% of adenomas and 80–85% of adenocarcinomas (Gupta and Dubois, 2001). Consequently, COX-2 emerged as a compelling therapeutic target in human CRC (Eberhart et al., 1994; Gupta and Dubois, 2001; Wang et al., 2005).

Targeting COX using NSAIDs inhibits its enzymatic activity and reduces PG expression, which is particularly relevant for PGs involved in tumor promotion during CRC progression, for instance, $PGF_{2\alpha}$ (Wang et al., 2005).

We exposed differentiated hCDMs and Caco-2 monolayers to increasing concentrations of the NSAIDs celecoxib (a COX-2 selective inhibitor) and sulindac (a non-selective COX-1 and COX-2 inhibitor) for 2, 6 and 24h (Fig. 5). The PD characteristics of both drugs are summarized in Table 1. In these experiments, monolayers were exposed from the apical side only to mimic oral administration, as shown in Fig. 5*a*.

We first assessed drug accumulation and estimated C_{cell} (total) and $C_{u,cell}$ (unbound) concentrations upon treatment with celecoxib (Fig. 5*b*, left) and sulindac (Fig. 5*b*, right) in hCDMs. Nominal incubation concentrations, as well as C_{cell} and $C_{u,cell}$, are compiled in Table 3.

Fig. 5*b* illustrates a clear relationship between nominal incubation concentrations and $C_{u,cell}$: as the incubation concentration increases, $C_{u,cell}$ also rises at the same time point for both NSAIDs. There appears to be no time dependency, regardless of concentration; cell accumulation occurs rapidly within the 0–2h window for both NSAIDs. Notably, sulindac displays a decrease in $C_{u,cell}$ between 2 and 6h, likely due to an experimental artifact, as all other unbound intracellular concentration profiles remain stable over time. Interestingly, while the C_{cell} values for celecoxib are significantly higher than those for sulindac, even at lower nominal incubation concentrations (Table 3), the unbound intracellular concentrations for celecoxib are much lower. This is attributed to the very low estimated $f_{u,cell}$ for celecoxib (0.0022 ± 0.0002; Table 3), which is roughly 79-fold lower than that of sulindac, leading to considerably lower $C_{u,cell}$ levels of celecoxib.

The abundance levels of $PGF_{2\alpha}$ (Fig. 5c_1), 15k $PGF_{2\alpha}$ (Fig. 5c_2), PGE_2+PGD_2 (Fig. 5c_3), and dhk PGE_2 (Fig. 5c_4), post-NSAID treatment confirmed that celecoxib exhibits a more pronounced effect in diminishing PG abundance compared to sulindac. Noteworthy, a clear concentration-dependent response was observed in hCDMs for celecoxib, though this response was less consistent and discernible in the Caco-2 system (e.g., abundance of PGE_2+PGD_2 in Caco-2 monolayers; Fig. 5c_3, right).

Conversely, sulindac appears less effective than celecoxib, demonstrating negligible activity in both *in vitro* systems across all tested conditions. This reduced efficacy is presumably due to sulindac being a prodrug that requires *in vivo* reduction to sulindac sulfide, its pharmacologically active metabolite (Brunell et al., 2011; Tinsley et al., 2009). If this step is compromised, sulindac remains inactive and fails to exert therapeutic effects (Tinsley et al., 2009).

Ultimately, the significantly lower $C_{u,cell}$ values of celecoxib compared to sulindac (Fig. 5*b*; Table 3)—influenced by the corresponding $f_{u,cell}$— indicate that celecoxib is the more potent drug of the two NSAIDs. It requires a far lower $C_{u,cell}$ to achieve PD effects than sulindac (Fig. 5$c_{1–4}$). At all timepoints, $C_{u,cell}$ levels for sulindac remain higher than those for celecoxib.

4. Conclusion

This proof-of-concept study evaluates the potential of differentiated hCDMs as an *in vitro* platform for investigating small molecule accumulation, toxicity, and PD, benchmarked against Caco-2 monolayers.

Differentiated hCDMs form polarized epithelial monolayers with physiologically relevant barrier properties. In toxicity assays, they show increased sensitivity to the EGFR-TKIs erlotinib and gefitinib, evidenced by lower IC_{20} values and $IC_{20}/30\times C_{max}$ ratios, while displaying reduced sensitivity to SN-38, indicated by higher IC_{20} and $IC_{20}/30\times C_{max}$, relative to Caco-2 monolayers. Investigations with irinotecan highlight the pivotal role of active efflux and metabolic processes in modulating

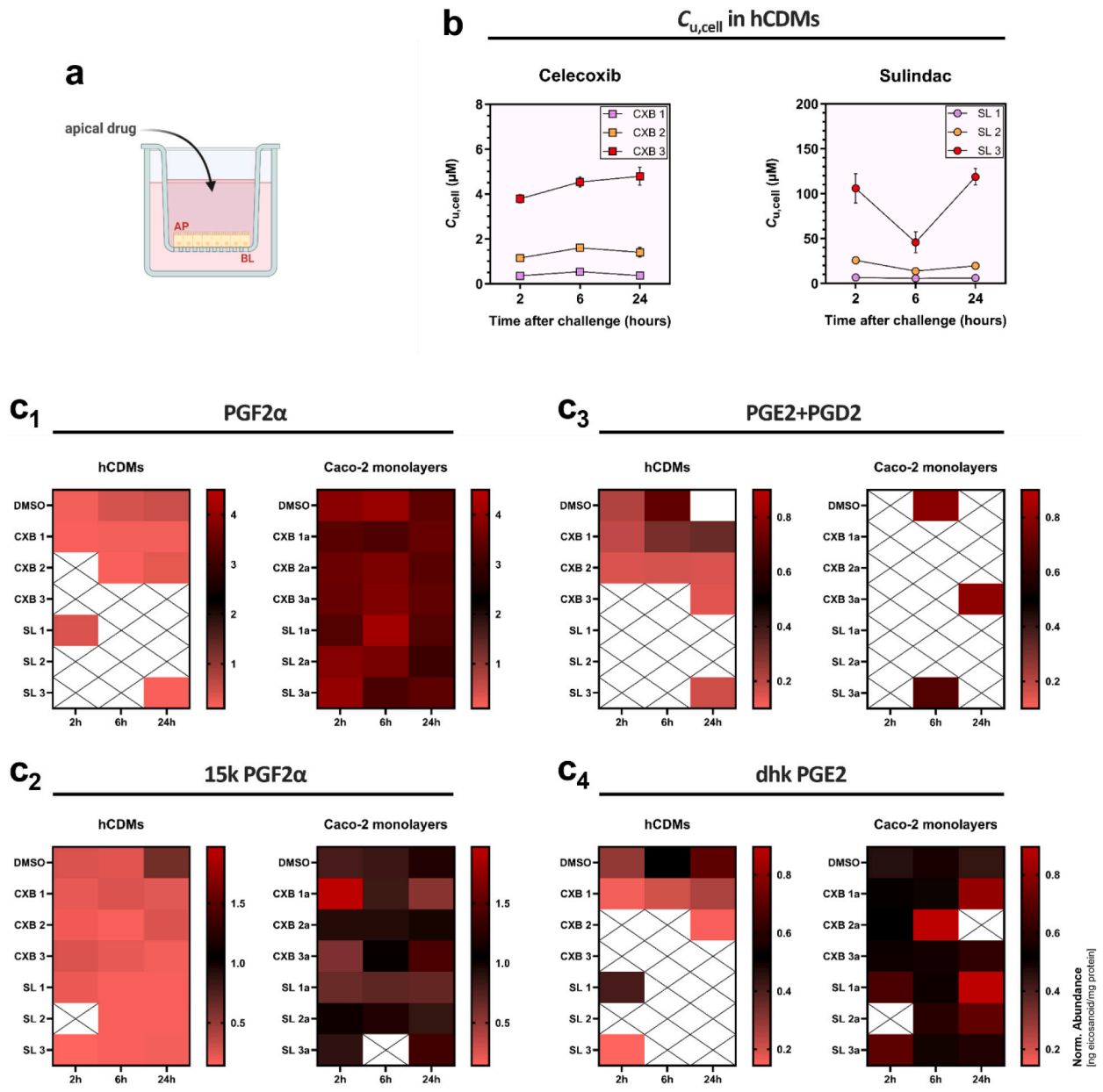

Fig. 5. Unbound intracellular concentration ($C_{u,cell}$) and eicosanoid signatures following NSAID exposure. (a) Schematic of drug exposure in PD and cell accumulation assays. Differentiated hCDMs and Caco-2 monolayers were treated with 3 concentrations of the NSAIDs celecoxib (CXB) and sulindac (SL) on the AP side. hCDMs were used at day 16 (day 5 of differentiation), and Caco-2 monolayers at day 21. **(b) $C_{u,cell}$ measurements after 2, 6, and 24-hour incubations with increasing CXB and SL concentrations in hCDMs.** For CXB (*left*): CXB 1 (lavender squares) – 19 µM, CXB 2 (orange squares) – 60 µM, and CXB 3 (red squares) – 190 µM; for SL (*right*): SL 1 (lavender circles) – 95 µM, SL 2 (orange circles) – 300 µM, and SL 3 (red circles) – 950 µM (refer to "hCDMs" in Table S7). 1, 2, and 3 indicate the nominal concentrations of CXB (squares) and SL (circles) during incubation, with the corresponding measured $C_{u,cell}$ values depicted in the plots. Data are shown as mean ± S.D. of three technical replicates ($n = 3$). $C_{u,cell}$, along with C_{cell} and $f_{u,cell}$ for both NSAIDs, are summarized in Table 3. **(c) Heatmap colors depicting median post-treatment abundance levels of selected eicosanoids. (c_1)** Prostaglandin F2α (PGF2α), **(c_2)** 15-keto prostaglandin F2α (15k PGF2α), **(c_3)** combined prostaglandins E2 and D2 (PGE2+PGD2), and **(c_4)** 13,14-dihydro-15-keto prostaglandin E2 (dhk PGE2), after treatment with CXB and SL. Nominal concentrations for hCDMs are the same as defined in (b); for Caco-2 monolayers: CXB 1a – 0.19 µM, CXB 2a – 1.90 µM, CXB 3a – 60 µM, SL 1a – 0.95 µM, SL 2a – 9.51 µM, and SL 3a – 300 µM (see "Caco-2 monolayers" in Table S7). The DMSO condition reflects baseline abundance levels in DMSO-treated (0.5%) medium. Abundance levels, represented by red double gradients, were measured at 2, 6, and 24h, normalized to total protein content, and expressed in ng eicosanoid/mg protein. Darker shades signify higher concentrations, and a cross symbol denotes levels below the LLOQ.

intracellular drug accumulation and toxicity, underscoring that accounting for efflux mechanisms and metabolism can sharpen *in vitro* toxicity predictions. Furthermore, hCDMs provide a colon-like representation of the PG pathway based on their baseline eicosanoid profiles, in contrast to the cancer-like abundance patterns observed in Caco-2 monolayers. PD analysis further reveals that celecoxib elicits a clear, dose-dependent reduction in PG abundance in hCDMs, an effect not discernible in the Caco-2 system.

Some limitations merit consideration. Relying on a single donor restricts evaluation of interindividual variability, while the relatively small, albeit clinically relevant, compound panel constrains generalizability. Future studies should include multiple patient colonoid-derived monolayers and a larger compound set to assess clinical relevance. Comparative work with monolayers from various intestinal regions (e.

g., duodenum) and differentiation states (proliferative versus differentiated) within the same donor could yield valuable insights. Although diarrhea remains the primary indicator of intestinal toxicity, its MoT and target cell types remain unclear. The absence of immune and smooth muscle cells, vasculature, and mechanical cues or flow, may limit the model's ability to capture certain mechanisms underlying drug-induced diarrhea (Peters et al., 2020). To our knowledge, the use of human colonic organotypic models to interrogate PD endpoints is unprecedented and warrants further investigation.

In summary, hCDMs emerge as a promising platform for integrated assessment of drug accumulation, toxicity, and PD, providing a more physiologically meaningful alternative to the widely adopted Caco-2 model. This approach also supports the ongoing shift toward NAMs in the pharmaceutical industry. Future efforts with CIVMs will further advance predictive safety, deepen mechanistic understanding, and potentially streamline drug development.

CRediT authorship contribution statement

Pedro G.M. Canhão: Writing – review & editing, Writing – original draft, Visualization, Validation, Project administration, Methodology, Investigation, Formal analysis, Data curation, Conceptualization. **Anny Smeuninx:** Writing – review & editing, Writing – original draft, Visualization, Methodology, Investigation, Formal analysis, Data curation. **Suzy Geerinckx:** Methodology, Investigation, Data curation. **Raymond Evers:** Writing – review & editing, Resources, Conceptualization. **Jan Snoeys:** Writing – review & editing, Supervision, Conceptualization. **Patrick Augustijns:** Writing – review & editing, Supervision, Resources, Project administration, Funding acquisition, Data curation, Conceptualization. **Stephanie Kourula:** Writing – review & editing, Supervision, Resources, Project administration, Funding acquisition, Data curation, Conceptualization.

Declaration of generative AI and AI-assisted technologies in the writing process

During the preparation of this work the authors used Gen AI by Johnson and Johnson (GPT-4o model) in order to check spelling and grammar. After using this tool/service, the authors reviewed and edited the content as needed and take full responsibility for the content of the publication.

Declaration of competing interest

Authors declare no conflicts of interest, financial or otherwise.

Acknowledgements

This work was funded by the European Union's Horizon 2020 Research and Innovation Program under the Marie Skłodowska-Curie Grant agreement no. 956851 (COLOTAN).

We thank Saro Mardirosian (Preclinical Sciences & Translational Safety, Johnson & Johnson, USA) for conducting the intracellular drug binding studies. We are also grateful to Stijn Van Asten (Preclinical Sciences & Translational Safety, Johnson & Johnson, Belgium) for his support in optimizing the LC–MS/MS parameters used to quantify our compound set in drug transport studies, and to Ferran Jardi (Preclinical Sciences & Translational Safety, Johnson & Johnson, Belgium) for reviewing the manuscript and providing expert input on toxicity. Lastly, we extend our appreciation to Marjolein Crabbe and Jan Serroyen (Discovery Statistics, Johnson & Johnson, Belgium) for the stimulating discussions on statistical analysis and dose-response curve fitting using 4PL nonlinear regression models to estimate IC_{20} values.

Appendix A. Supplementary data

Supplementary data to this article can be found online at https://doi.org/10.1016/j.tiv.2026.106221.

Data availability

The data supporting the conclusions of this article is available within the main text and supplementary materials. Further inquiries can be addressed to the corresponding author.

References

Ambrosini, Y.M., Park, Y., Jergens, A.E., Shin, W., Min, S., Atherly, T., Borcherding, D.C., Jang, J., Allenspach, K., Mochel, J.P., Kim, H.J., 2020. Recapitulation of the accessible interface of biopsy-derived canine intestinal organoids to study epithelial-luminal interactions. PLoS One 15, 1–17. https://doi.org/10.1371/journal.pone.0231423.

Arian, C., Mahony, E.O., MacDonald, J.W., Bammler, T.K., Donowitz, M., Kelly, E.J., Thummel, K.E., 2024. Human enteroid monolayers: a novel, functionally-stable model for investigating oral drug disposition. Drug Metab. Dispos. 52, 1–43. https://doi.org/10.1124/dmd.124.001551.

Ayehunie, S., Landry, T., Stevens, Z., Armento, A., Hayden, P., Klausner, M., 2018. Human primary cell-based organotypic microtissues for modeling small intestinal drug absorption. Pharm. Res. 35, 1–18. https://doi.org/10.1007/s11095-018-2362-0.

Barbier, S., Beaufils, B., de Miguel, R., Reyre, M., Le Meitour, Y., Lortie, A., de Boisferon, M.H., Chaumeron, S., Espirito, A., Fossati, L., Lagarde, P., Klinz, S., Thiagalingam, A., Lezmi, S., Meyer-Losic, F., 2023. Liposomal irinotecan shows a larger therapeutic index than non-liposomal irinotecan in patient-derived xenograft models of pancreatic cancer. Oncol. Ther. 11 (1), 111–128. https://doi.org/10.1007/s40487-022-00215-2.

Belair, D.G., Visconti, R.J., Hong, M., Marella, M., Peters, M.F., Scott, C.W., Kolaja, K.L., 2020. Human ileal organoid model recapitulates clinical incidence of diarrhea associated with small molecule drugs. Toxicol. in Vitro 68, 1–8. https://doi.org/10.1016/j.tiv.2020.104928.

Brunell, D., Sagher, D., Kesaraju, S., Brot, N., Weissbach, H., 2011. Studies on the metabolism and biological activity of the epimers of sulindac. Drug Metab. Dispos. 39, 1014–1021. https://doi.org/10.1124/dmd.110.037663.

Calvo, E., Malik, S.N., Siu, L.L., Baillargeon, G.M., Irish, J., Chin, S.F., Santabarbara, P., Kreisberg, J.I., Rowinsky, E.K., Hidalgo, M., 2007. Assessment of erlotinib pharmacodynamics in tumors and skin of patients with head and neck cancer. Ann. Oncol. 18 (4), 761–767. https://doi.org/10.1093/annonc/mdl495.

CAMPTOSAR®, 2014. Prescribing Information. Pfizer Inc. 1–39.

Canhão, P.G.M., Snoeys, J., Geerinckx, S., van Heerden, M., Van den Bergh, A., Holm, C., Markus, J., Ayehunie, S., Monshouwer, M., Evers, R., Augustijns, P., Kourula, S., 2025. Human organotypic colon in vitro microtissue: unveiling a new window into colonic drug disposition. Eur. J. Pharm. Sci. 209, 1–16. https://doi.org/10.1016/j.ejps.2025.107025.

CELEBREX®, 2008. Prescribing Information. Pfizer Inc. 1–16.

CELEBREX®, 1998. Clinical Pharmacology and Biopharmaceutics Review. US FDA 1–21.

Chabot, G.G., Abigerges, D., Catimel, G., Culine, S., de Forni, M., Extra, J.-M., Mahjoubi, M., Hérait, P., Armand, J.-P., Bugat, R., Clavel, M., Marty, M.E., 1995. Population pharmacokinetics and pharmacodynamics of irinotecan (CPT-11) and active metabolite SN-38 during phase I trials. Ann. Oncol. 6, 141–151. https://doi.org/10.1093/oxfordjournals.annonc.a059109.

Cirit, M., Stokes, C.L., 2018. Maximizing the impact of microphysiological systems with in vitro–in vivo translation. Lab Chip 18, 1831–1837. https://doi.org/10.1039/C8LC00039E.

Clark, M., Steger-Hartmann, T., 2018. A big data approach to the concordance of the toxicity of pharmaceuticals in animals and humans. Regul. Toxicol. Pharmacol. 96, 94–105. https://doi.org/10.1016/j.yrtph.2018.04.018.

CLINORIL®, 2010. Prescribing Information. Merck Co. Inc 1–17.

Combes, O., Barré, J., Duché, J.C., Vernillet, L., Archimbaud, Y., Marietta, M.P., Tillement, J.P., Urien, S., 2000. In vitro binding and partitioning of irinotecan (CPT-11) and its metabolite, SN-38, in human blood. Invest. New Drugs 18, 1–5. https://doi.org/10.1023/A:1006379730137.

d'Aldebert, E., Quaranta, M., Sébert, M., Bonnet, D., Kirzin, S., Portier, G., Duffas, J.P., Chabot, S., Lluel, P., Allart, S., Ferrand, A., Alric, L., Racaud-Sultan, C., Mas, E., Deraison, C., Vergnolle, N., 2020. Characterization of human colon organoids from inflammatory bowel disease patients. Front. Cell Dev. Biol. 8, 1–13. https://doi.org/10.3389/fcell.2020.00363.

Denlinger, C.S., Blanchard, R., Xu, L., Bernaards, C., Litwin, S., Spittle, C., Berg, D.J., McLaughlin, S., Redlinger, M., Dorr, A., Hambleton, J., Holden, S., Kearns, A., Kenkare-Mitra, S., Lum, B., Meropol, N.J., O'Dwyer, P.J., 2009. Pharmacokinetic analysis of irinotecan plus bevacizumab in patients with advanced solid tumors. Cancer Chemother. Pharmacol. 65, 97–105. https://doi.org/10.1007/s00280-009-1008-7.

Eaton, A., Iasonos, A., Gounder, M.M., Pamer, E.G., Drilon, A., Vulih, D., Smith, G.L., Ivy, S.P., Spriggs, D.R., Hyman, D.M., 2016. Toxicity attribution in phase I trials: evaluating the effect of dose on the frequency of related and unrelated toxicities. Clin. Cancer Res. 22, 553–559. https://doi.org/10.1158/1078-0432.CCR-15-0339.

Eberhart, C.E., Coffey, R.J., Radhika, A., Giardiello, F.M., Ferrenbach, S., DuBois, R.N., 1994. Up-regulation of cyclooxygenase 2 gene expression in human colorectal adenomas and adenocarcinomas. Gastroenterology 107, 1183–1188. https://doi.org/10.1016/0016-5085(94)90246-1.

Ekert, J.E., Deakyne, J., Pribul-Allen, P., Terry, R., Schofield, C., Jeong, C.G., Storey, J., Mohamet, L., Francis, J., Naidoo, A., Amador, A., Klein, J.L., Rowan, W., 2020. Recommended guidelines for developing, qualifying, and implementing complex in vitro models (CIVMs) for drug discovery. SLAS Discov. 25, 1174–1190. https://doi.org/10.1177/2472555220923332.

Englund, G., Rorsman, F., Rönnblom, A., Karlbom, U., Lazorova, L., Gråsjö, J., Kindmark, A., Artursson, P., 2006. Regional levels of drug transporters along the human intestinal tract: Co-expression of ABC and SLC transporters and comparison with Caco-2 cells. Eur. J. Pharm. Sci. 29, 269–277. https://doi.org/10.1016/j.ejps.2006.04.010.

Federer, C., Yoo, M., Tan, A.C., 2016. Big data mining and adverse event pattern analysis in clinical drug trials. Assay Drug Dev. Technol. 14, 557–566. https://doi.org/10.1089/adt.2016.742.

Finkbeiner, S.R., Freeman, J.J., Wieck, M.M., El-Nachef, W., Altheim, C.H., Tsai, Y.-H., Huang, S., Dyal, R., White, E.S., Grikscheit, T.C., Teitelbaum, D.H., Spence, J.R., 2015. Generation of tissue-engineered small intestine using embryonic stem cell-derived human intestinal organoids. Biol. Open 4, 1462–1472. https://doi.org/10.1242/bio.013235.

Fornai, M., Antonioli, L., Colucci, R., Pellegrini, C., Giustarini, G., Testai, L., Martelli, A., Matarangasi, A., Natale, G., Calderone, V., Tuccori, M., Scarpignato, C., Blandizzi, C., 2014. NSAID-induced enteropathy : are the currently available selective COX-2 inhibitors all the same? J. Pharmacol. Exp. Ther. 348, 86–95. https://doi.org/10.1124/jpet.113.207118.

Gong, L., Thorn, C.F., Bertagnolli, M.M., Grosser, T., Altman, R.B., Klein, T.E., 2012. Celecoxib pathways: pharmacokinetics and pharmacodynamics. Pharmacogenet. Genomics 22, 310–318. https://doi.org/10.1097/FPC.0b013e32834f94cb.

Gupta, R.A., Dubois, R.N., 2001. Colorectal cancer prevention and treatment by inhibition of cyclooxygenase-2. Nat. Rev. Cancer 1, 11–21. https://doi.org/10.1038/35094017.

Hammer, T., Langholz, E., 2020. The epidemiology of inflammatory bowel disease: balance between East and West? A narrative review. Dig Med. Res. 3, 48. https://doi.org/10.21037/dmr-20-149.

Hartung, T., 2024. The (misleading) role of animal models in drug development. Front. Drug Discov. 4, 1–18. https://doi.org/10.3389/fddsv.2024.1355044.

Hartung, T., Smirnova, L., 2025. A path forward advancing microphysiological systems. ALTEX Alternat. Anim. Exp. 42, 183–203. https://doi.org/10.14573/altex.2504091.

Hirose, T., Fujita, K., Kusumoto, S., Oki, Y., Murata, Y., Sugiyama, T., Ishida, H., Shirai, T., Nakashima, M., Yamaoka, T., Okuda, K., Ohmori, T., Sasaki, Y., 2016. Association of pharmacokinetics and pharmacogenomics with safety and efficacy of gefitinib in patients with EGFR mutation positive advanced non-small cell lung cancer. Lung Cancer 93, 69–76. https://doi.org/10.1016/j.lungcan.2016.01.005.

Homan, K.A., 2023. Industry adoption of organoids and organs-on-chip technology : toward a paradox of choice. Adv. Biol. 2200334, 1–5. https://doi.org/10.1002/adbi.202200334.

Honeywell, R.J., Kathmann, I., Giovannetti, E., Tibaldi, C., Smit, E.F., Rovithi, M.N., Verheul, H.M.W., Peters, G.J., 2020. Epithelial transfer of the tyrosine kinase inhibitors erlotinib, gefitinib, afatinib, crizotinib, sorafenib, sunitinib, and dasatinib: implications for clinical resistance. Cancers (Basel) 12, 1–18. https://doi.org/10.3390/cancers12113322.

Hubatsch, I., Ragnarsson, E.G.E., Artursson, P., 2007. Determination of drug permeability and prediction of drug absorption in Caco-2 monolayers. Nat. Protoc. 2, 2111–2119. https://doi.org/10.1038/nprot.2007.303.

IRESSA®, 2018. Prescribing Information. AstraZeneca Pharm. LP 1–17.

Jelinsky, S.A., Derksen, M., Bauman, E., Verissimo, C.S., van Dooremalen, W.T.M., Roos, J.L., Barón, C.H., Caballero-Franco, C., Johnson, B.G., Rooks, M.G., Pott, J., Oldenburg, B., Vries, R.G.J., Boj, S.F., Kasaian, M.T., Pourfarzad, F., Rosadini, C.V., 2023. Molecular and functional characterization of human intestinal organoids and monolayers for modeling epithelial barrier. Inflamm. Bowel Dis. 29, 195–206. https://doi.org/10.1093/ibd/izac212.

Khalil, A.S., Jaenisch, R., Mooney, D.J., 2020. Engineered tissues and strategies to overcome challenges in drug development. Adv. Drug Deliv. Rev. 158, 116–139. https://doi.org/10.1016/j.addr.2020.09.012.

Klein, J.A., Heidmann, J.D., Kiyota, T., Fullerton, A., Homan, K.A., Co, J.Y., 2025. The differentiation state of small intestinal organoid models influences prediction of drug-induced toxicity. Front. Cell Dev. Biol. 13, 1–10. https://doi.org/10.3389/fcell.2025.1508820.

Kourula, S., Derksen, M., Jardi, F., Jonkers, S., van Heerden, M., Verboven, P., Theuns, V., Van Asten, S., Huybrechts, T., Kunze, A., Frazer-Mendelewska, E., Lai, K. W., Overmeer, R., Roos, J.L., Vries, R.G.J., Boj, S.F., Monshouwer, M., Pourfarzad, F., Snoeys, J., 2023. Intestinal organoids as an in vitro platform to characterize disposition, metabolism, and safety profile of small molecules. Eur. J. Pharm. Sci. 188, 1–15. https://doi.org/10.1016/j.ejps.2023.106481.

Kraiczy, J., Nayak, K.M., Howell, K.J., Ross, A., Forbester, J., Salvestrini, C., Mustata, R., Perkins, S., Andersson-Rolf, A., Leenen, E., Liebert, A., Vallier, L., Rosenstiel, P.C., Stegle, O., Dougan, G., Heuschkel, R., Koo, B.K., Zilbauer, M., 2019. DNA methylation defines regional identity of human intestinal epithelial organoids and undergoes dynamic changes during development. Gut 68, 49–61. https://doi.org/10.1136/gutjnl-2017-314817.

Kus, M., Ibragimow, I., Piotrowska-Kempisty, H., 2023. Caco-2 cell line standardization with pharmaceutical requirements and in vitro model suitability for permeability assays. Pharmaceutics 15, 1–15. https://doi.org/10.3390/pharmaceutics15112523.

Kwon, O., Jung, K.B., Lee, K.R., Son, Y.S., Lee, H., Kim, J.J., Kim, K., Lee, S., Song, Y.K., Jung, J., Park, K., Kim, D.S., Son, M.J., Lee, M.O., Han, T.S., Cho, H.S., Oh, S.J., Chung, H., Kim, S.H., Chung, K.S., Kim, J., Jung, C.R., Son, M.Y., 2021. The development of a functional human small intestinal epithelium model for drug absorption. Sci. Adv. 7, 1–18. https://doi.org/10.1126/sciadv.abh1586.

Larregieu, C.A., Benet, L.Z., 2013. Drug discovery and regulatory considerations for improving in silico and in vitro predictions that use caco-2 as a surrogate for human intestinal permeability measurements. AAPS J. 15, 483–497. https://doi.org/10.1208/s12248-013-9456-8.

Lechuga, S., Braga-Neto, M.B., Naydenov, N.G., Rieder, F., Ivanov, A.I., 2023. Understanding disruption of the gut barrier during inflammation: should we abandon traditional epithelial cell lines and switch to intestinal organoids? Front. Immunol. 14, 1–15. https://doi.org/10.3389/fimmu.2023.1108289.

Lemmens, G., Van Camp, A., Kourula, S., Vanuytsel, T., Augustijns, P., 2021. Drug disposition in the lower gastrointestinal tract: targeting and monitoring. Pharmaceutics 13, 1–53. https://doi.org/10.3390/pharmaceutics13020161.

Li, Y., Meng, Q., Yang, M., Liu, D., Hou, X., Tang, L., Wang, X., Lyu, Y., Chen, X., Liu, K., Yu, A.M., Zuo, Z., Bi, H., 2019. Current trends in drug metabolism and pharmacokinetics. Acta Pharm. Sin. B 9, 1113–1144. https://doi.org/10.1016/j.apsb.2019.10.001.

Lin, Z., Will, Y., 2012. Evaluation of drugs with specific organ toxicities in organ-specific cell lines. Toxicol. Sci. 126, 114–127. https://doi.org/10.1093/toxsci/kfr339.

Lohasz, C., Loretan, J., Sterker, D., Görlach, E., Renggli, K., Argast, P., Frey, O., Wiesmann, M., Wartmann, M., Rausch, M., Hierlemann, A., 2021. A microphysiological cell-culturing system for pharmacokinetic drug exposure and high-resolution imaging of arrays of 3D microtissues. Front. Pharmacol. 12, 1–17. https://doi.org/10.3389/fphar.2021.785851.

Lombardo, F., Berellini, G., Obach, R.S., 2018. Trend analysis of a database of intravenous pharmacokinetic parameters in humans for 1352 drug compounds. Drug Metab. Dispos. 46, 1466–1477. https://doi.org/10.1124/dmd.118.082966.

Mahe, M.M., Sundaram, N., Watson, C.L., Shroyer, N.F., Helmrath, M.A., 2015. Establishment of human epithelial enteroids and colonoids from whole tissue and biopsy. J. Vis. Exp. 2015, 1–13. https://doi.org/10.3791/52483.

Maniewska, J., Jeżewska, D., 2021. Non-steroidal anti-inflammatory drugs in colorectal cancer chemoprevention. Cancers (Basel) 13, 1–18. https://doi.org/10.3390/cancers13040594.

Marcellinaro, R., Spoletini, D., Grieco, M., Avella, P., Cappuccio, M., Troiano, R., Lisi, G., Garbarino, G.M., Carlini, M., 2024. Colorectal cancer: current updates and future perspectives. J. Clin. Med. 13, 1–12. https://doi.org/10.3390/jcm13010040.

Markus, J., Landry, T., Stevens, Z., Scott, H., Llanos, P., Debatis, M., Armento, A., Klausner, M., Ayehunie, S., 2021. Human small intestinal organotypic culture model for drug permeation, inflammation, and toxicity assays. In Vitro Cell Dev. Biol. Anim. 57, 160–173. https://doi.org/10.1007/s11626-020-00526-6.

Mateus, A., Matsson, P., Artursson, P., 2013. Rapid measurement of intracellular unbound drug concentrations. Mol. Pharm. 10, 2467–2478. https://doi.org/10.1021/mp4000822.

Mateus, A., Treyer, A., Wegler, C., Karlgren, M., Matsson, P., Artursson, P., 2017. Intracellular drug bioavailability: a new predictor of system dependent drug disposition. Sci. Rep. 7, 1–12. https://doi.org/10.1038/srep43047.

Miller, R., Ewy, W., Corrigan, B.W., Ouellet, D., Hermann, D., Kowalski, K.G., Lockwood, P., Koup, J.R., Donevan, S., El-Kattan, A., Li, C.S.W., Werth, J.L., Feltner, D.E., Lalonde, R.L., 2005. How modeling and simulation have enhanced decision making in new drug development. J. Pharmacokinet. Pharmacodyn. 32, 185–197. https://doi.org/10.1007/s10928-005-0074-7.

Mitrofanova, O., Nikolaev, M., Xu, Q., Broguiere, N., Cubela, I., Camp, J.G., Bscheider, M., Lutolf, M.P., 2024. Bioengineered human colon organoids with in vivo-like cellular complexity and function. Cell Stem Cell 31 (8), 1175–1186.e7. https://doi.org/10.1016/j.stem.2024.05.007.

Mohammadi, S., Morell-Perez, C., Wright, C.W., Wyche, T.P., 2021. Assessing donor-to-donor variability in human intestinal organoid cultures. Stem Cell Reports 16, 2364–2378. https://doi.org/10.1016/j.stemcr.2021.07.016.

Monticello, T.M., Jones, T.W., Dambach, D.M., Potter, D.M., Bolt, M.W., Liu, M., Keller, D.A., Hart, T.K., Kadambi, V.J., 2017. Current nonclinical testing paradigm enables safe entry to First-In-Human clinical trials: the IQ consortium nonclinical to clinical translational database. Toxicol. Appl. Pharmacol. 334, 100–109. https://doi.org/10.1016/j.taap.2017.09.006.

Morgan, S.J., Elangbam, C.S., Berens, S., Janovitz, E., Vitsky, A., Zabka, T., Conour, L., 2013. Use of animal models of human disease for nonclinical safety assessment of novel pharmaceuticals. Toxicol. Pathol. 41, 508–518. https://doi.org/10.1177/0192623312457273.

Müller, J., Keiser, M., Drozdzik, M., Oswald, S., 2017. Expression, regulation and function of intestinal drug transporters: an update. Biol. Chem. 398, 175–192. https://doi.org/10.1515/hsz-2016-0259.

Murray, K., Hoad, C.L., Mudie, D.M., Wright, J., Heissam, K., Abrehart, N., Pritchard, S. E., Al Atwah, S., Gowland, P.A., Garnett, M.C., Amidon, G.E., Spiller, R.C., Amidon, G.L., Marciani, L., 2017. Magnetic resonance imaging quantification of fasted state colonic liquid pockets in healthy humans. Mol. Pharm. 14, 2629–2638. https://doi.org/10.1021/acs.molpharmaceut.7b00095.

Nguyen, T.V., Alfarsi, A., Nguyen, H.T., Davidson, G., Lloyd, N.D.R., Kumar, A., 2025. Metabolic disruptions induced by low concentrations of DMSO in RTgill-W1 fish cells: the importance of solvent controls in in vitro studies. Aquat. Toxicol. 283, 1–11. https://doi.org/10.1016/j.aquatox.2025.107354.

Nickerson, K.P., Llanos-Chea, A., Ingano, L., Serena, G., Miranda-Ribera, A., Perlman, M., Lima, R., Sztein, M.B., Fasano, A., Senger, S., Faherty, C.S., 2021. A versatile human intestinal organoid-derived epithelial monolayer model for the study of enteric

pathogens. Microbiol. Spectrum 9, 1–17. https://doi.org/10.1128/spectrum.00003-21.
Nugent, K.P., Spigelman, A.D., Phillips, R.K., 1996. Tissue prostaglandin levels in familial adenomatous polyposis patients treated with sulindac. Dis. Colon Rectum 39, 659–662. https://doi.org/10.1007/BF02056946.
O'Mahony, E.T., Arian, C.M., Aryeh, K.S., Wang, K., Thummel, K.E., Kelly, E.J., 2025. Human intestinal enteroids: nonclinical applications for predicting oral drug disposition, toxicity, and efficacy. Pharmacol. Ther. 108879, 1–74. https://doi.org/10.1016/j.pharmthera.2025.108879.
Ölander, M., Wiśniewski, J.R., Matsson, P., Lundquist, P., Artursson, P., 2016. The proteome of filter-grown Caco-2 cells with a focus on proteins involved in drug disposition. J. Pharm. Sci. 105, 817–827. https://doi.org/10.1016/j.xphs.2015.10.030.
Olson, H., Betton, G., Robinson, D., Thomas, K., Monro, A., Kolaja, G., Lilly, P., Sanders, J., Sipes, G., Bracken, W., Dorato, M., Van Deun, K., Smith, P., Berger, B., Heller, A., 2000. Concordance of the toxicity of pharmaceuticals in humans and in animals. Regul. Toxicol. Pharmacol. 32, 56–67. https://doi.org/10.1006/rtph.2000.1399.
Panse, N., Gerk, P.M., 2022. The Caco-2 model: modifications and enhancements to improve efficiency and predictive performance. Int. J. Pharm. 624, 1–11. https://doi.org/10.1016/j.ijpharm.2022.122004.
Parente, I.A., Chiara, L., Bertoni, S., 2024. Exploring the potential of human intestinal organoids: applications, challenges, and future directions. Life Sci. 352, 1–14. https://doi.org/10.1016/j.lfs.2024.122875.
Parvez, M.M., Basit, A., Jariwala, P.B., Gaborik, Z., Kis, E., Heyward, S., Redinbo, M.R., Prasad, B., 2021. Quantitative investigation of irinotecan metabolism, transport, and gut microbiome activation. Drug Metab. Dispos. 49, 683–693. https://doi.org/10.1124/DMD.121.000476.
Peters, M.F., Landry, T., Pin, C., Maratea, K., Dick, C., Wagoner, M.P., Choy, A.L., Barthlow, H., Snow, D., Stevens, Z., Armento, A., Scott, C.W., Ayehunie, S., 2019. Human 3D gastrointestinal microtissue barrier function as a predictor of drug-induced diarrhea. Toxicol. Sci. 168, 3–17. https://doi.org/10.1093/toxsci/kfy268.
Peters, M.F., Choy, A.L., Pin, C., Leishman, D.J., Moisan, A., Ewart, L., Guzzie-Peck, P.J., Sura, R., Keller, D.A., Scott, C.W., Kolaja, K.L., 2020. Developing in vitro assays to transform gastrointestinal safety assessment: potential for microphysiological systems. Lab Chip 20, 1177–1190. https://doi.org/10.1039/c9lc01107b.
Pike, C.M., Zwarycz, B., McQueen, B.E., Castillo, M., Barron, C., Morowitz, J.M., Levi, J. A., Phadke, D., Balik-Meisner, M., Mav, D., Shah, R., Cunningham Glasspoole, D.L., Laetham, R., Thelin, W., Bunger, M.K., Boazak, E.M., 2024. Characterization and optimization of variability in a human colonic epithelium culture model. ALTEX Alternat. Anim. Exp. 41, 425–438. https://doi.org/10.14573/altex.2309221.
Pike, C.M., Levi, J.A., Boone, L.A., Peddibhotla, S., Johnson, J., Zwarycz, B., Bunger, M. K., Thelin, W., Boazak, E.M., 2025. High-throughput assay for predicting diarrhea risk using a 2D human intestinal stem cell-derived model. Toxicol. in Vitro 106, 1–11. https://doi.org/10.1016/j.tiv.2025.106040.
Pleguezuelos-Manzano, C., Puschhof, J., van den Brink, S., Geurts, V., Beumer, J., Clevers, H., 2020. Establishment and culture of human intestinal organoids derived from adult stem cells. Curr. Protoc. Immunol. 130, 1–24. https://doi.org/10.1002/cpim.106.
Posadas, E.M., Liel, M.S., Kwitkowski, V., Minasian, L., Godwin, A.K., Hussain, M.M., Espina, V., Wood, B.J., Steinberg, S.M., Kohn, E.C., 2007. A phase II and pharmacodynamic study of gefitinib in patients with refractory or recurrent epithelial ovarian cancer. Cancer 109 (7), 1323–1330. https://doi.org/10.1002/cncr.22545.
Prados, M.D., Lamborn, K.R., Chang, S., Burton, E., Butowski, N., Malec, M., Kapadia, A., Rabbitt, J., Page, M.S., Fedoroff, A., Xie, D., Kelley, S.K., 2006. Phase 1 study of erlotinib HCl alone and combined with temozolomide in patients with stable or recurrent malignant glioma1. Neuro. Oncol. 8, 67–78. https://doi.org/10.1215/S1522851705000451.
Press, B., Di Grandi, D., 2008. Permeability for intestinal absorption: Caco-2 assay and related issues. Curr. Drug Metab. 9, 893–900. https://doi.org/10.2174/138920008786485119.
Pretorius, E., Bouic, P.J.D., 2009. Permeation of four oral drugs through human intestinal mucosa. AAPS PharmSciTech 10, 270–275. https://doi.org/10.1208/s12249-009-9207-4.
Qualtrough, D., Kaidi, A., Chell, S., Jabbour, H.N., Williams, A.C., Paraskeva, C., 2007. Prostaglandin F2α stimulates motility and invasion in colorectal tumor cells. Int. J. Cancer 121, 734–740. https://doi.org/10.1002/ijc.22755.
Reid, J.M., Mandrekar, S.J., Carlson, E.C., Harmsen, W.S., Green, E.M., McGovern, R.M., Szabo, E., Ames, M.M., Boring, D., Limburg, P.J., Network, for the C.P., 2008. Comparative Bioavailability of Sulindac in Capsule and Tablet Formulations. Cancer Epidemiol. Biomarkers Prev. 17, 674–679. https://doi.org/10.1158/1055-9965.EPI-07-2510.
Riccardi, K., Li, Z., Brown, J.A., Gorgoglione, M.F., Niosi, M., Gosset, J., Huard, K., Erion, D.M., Di, L., 2016. Determination of unbound partition coefficient and in vitro-in vivo extrapolation for SLC13A transporter-mediated uptake. Drug Metab. Dispos. 44, 1633–1642. https://doi.org/10.1124/dmd.116.071837.
Riccardi, K., Ryu, S., Lin, J., Yates, P., Tess, D., Li, R., Singh, D., Holder, B.R., Kapinos, B., Chang, G., Di, L., 2018. Comparison of species and cell-type differences in fraction unbound of liver tissues, hepatocytes, and cell lines. Drug Metab. Dispos. 46, 415–421. https://doi.org/10.1124/dmd.117.079152.
Ryu, S., Tess, D., Chang, G., Keefer, C., Burchett, W., Steeno, G.S., Novak, J.J., Patel, R., Atkinson, K., Riccardi, K., Di, L., 2020. Evaluation of fraction unbound across 7 tissues of 5 species. J. Pharm. Sci. 109, 1178–1190. https://doi.org/10.1016/j.xphs.2019.10.060.
Sato, T., Vries, R.G., Snippert, H.J., Van De Wetering, M., Barker, N., Stange, D.E., Van Es, J.H., Abo, A., Kujala, P., Peters, P.J., Clevers, H., 2009. Single Lgr5 stem cells build crypt-villus structures in vitro without a mesenchymal niche. Nature 459, 262–265. https://doi.org/10.1038/nature07935.
Sato, T., Stange, D.E., Ferrante, M., Vries, R.G.J., Van Es, J.H., Van Den Brink, S., Van Houdt, W.J., Pronk, A., Van Gorp, J., Siersema, P.D., Clevers, H., 2011. Long-term expansion of epithelial organoids from human colon, adenoma, adenocarcinoma, and Barrett's epithelium. Gastroenterology 141, 1762–1772. https://doi.org/10.1053/j.gastro.2011.07.050.
Schiller, C., Fröhlich, C.-P., Giessmann, T., Siegmund, W., Mönnikes, H., Hosten, N., Weitschies, W., 2005. Intestinal fluid volumes and transit of dosage forms as assessed by magnetic resonance imaging. Aliment. Pharmacol. Ther. 22, 971–979. https://doi.org/10.1111/j.1365-2036.2005.02683.x.
Shah, R., Lester, J.F., 2020. Tyrosine kinase inhibitors for the treatment of EGFR mutation-positive non–small-cell lung cancer: a clash of the generations. Clin. Lung Cancer 21, e216–e228. https://doi.org/10.1016/j.cllc.2019.12.003.
Signore, M.A., De Pascali, C., Giampetruzzi, L., Siciliano, P.A., Francioso, L., 2021. Gut-on-Chip microphysiological systems: latest advances in the integration of sensing strategies and adoption of mature detection mechanisms. Sens. Biosens. Res. 33, 1–26. https://doi.org/10.1016/j.sbsr.2021.100443.
Siissalo, S., Zhang, H., Stilgenbauer, E., Kaukonen, A.M., Hirvonen, J., Finel, M., 2008. The expression of most UDP-glucuronosyltransferases (UGTs) is increased significantly during Caco-2 cell differentiation, whereas UGT1A6 is highly expressed also in undifferentiated cells. Drug Metab. Dispos. 36, 2331–2336. https://doi.org/10.1124/dmd.108.022335.
Smith, N.F., Figg, W.D., Sparreboom, A., 2006. Pharmacogenetics of irinotecan metabolism and transport: an update. Toxicol. in Vitro 20, 163–175. https://doi.org/10.1016/j.tiv.2005.06.045.
Song, J., Liu, X., Wu, J., Meehan, M.J., Blevitt, J.M., Dorrestein, P.C., Milla, M.E., 2013. A highly efficient, high-throughput lipidomics platform for the quantitative detection of eicosanoids in human whole blood. Anal. Biochem. 433, 181–188. https://doi.org/10.1016/j.ab.2012.10.022.
Srinivasan, B., Kolli, A.R., Esch, M.B., Abaci, H.E., Shuler, M.L., Hickman, J.J., 2015. TEER measurement techniques for in vitro barrier model systems. J. Lab. Autom. 20, 107–126. https://doi.org/10.1177/2211068214561025.
Steinway, S.N., Saleh, J., Koo, B.K., Delacour, D., Kim, D.H., 2020. Human microphysiological models of intestinal tissue and gut microbiome. Front. Bioeng. Biotechnol. 8, 1–17. https://doi.org/10.3389/fbioe.2020.00725.
Sun, H., Chow, E.C.Y., Liu, S., Du, Y., Pang, K.S., 2008. The Caco-2 cell monolayer: usefulness and limitations. Expert Opin. Drug Metab. Toxicol. 4, 395–411. https://doi.org/10.1517/17425255.4.4.395.
Sun, D., Gao, W., Hu, H., Zhou, S., 2022. Why 90% of clinical drug development fails and how to improve it? Acta Pharm. Sin. B 12, 3049–3062. https://doi.org/10.1016/j.apsb.2022.02.002.
Tamaki, C., Nagayama, T., Hashiba, M., Fujiyoshi, M., Hizue, M., Kodaira, H., Nishida, M., Suzuki, K., Takashima, Y., Ogino, Y., Yasugi, D., Yoneta, Y., Hisada, S., Ohkura, T., Nakamura, K., 2013. Potentials and limitations of nonclinical safety assessment for predicting clinical adverse drug reactions: correlation analysis of 142 approved drugs in Japan. J. Toxicol. Sci. 38, 581–598. https://doi.org/10.2131/jts.38.581.
Tanaka, Y., Goto, T., Kataoka, M., Sakuma, S., Yamashita, S., 2015. Impact of luminal fluid volume on the drug absorption after oral administration: analysis based on in vivo drug concentration-time profile in the gastrointestinal tract. J. Pharm. Sci. 104, 3120–3127. https://doi.org/10.1002/jps.24433.
Tanaka, K., Mochizuki, T., Baba, S., Kawai, S., Nakano, K., Tachibana, T., Uchimura, K., Kato, A., Miyayama, T., Yamaguchi, T., Nishihara, H., Terao, K., Kato, Y., 2025. Robust and reproducible human intestinal organoid-derived monolayer model for analyzing drug absorption. Sci. Rep. 15, 1–21. https://doi.org/10.1038/s41598-025-95823-z.
Tannergren, C., Bergendal, A., Lennernäs, H., Abrahamsson, B., 2009. Toward an increased understanding of the barriers to colonic drug absorption in humans: implications for early controlled release candidate assessment. Mol. Pharm. 6, 60–73. https://doi.org/10.1021/mp800261a.
TARCEVA®, 2010. Prescribing Information. OSI Pharm. Inc., Genentech, Inc 1–24.
Teft, W.A., Welch, S., Lenehan, J., Parfitt, J., Choi, Y.H., Winquist, E., Kim, R.B., 2015. OATP1B1 and tumour OATP1B3 modulate exposure, toxicity, and survival after irinotecan-based chemotherapy. Br. J. Cancer 112, 857–865. https://doi.org/10.1038/bjc.2015.5.
Thun, M.J., Henley, S.J., Patrono, C., 2002. Nonsteroidal anti-inflammatory drugs as anticancer agents: mechanistic, pharmacologic, and clinical issues. JNCI J. Natl. Cancer Inst. 94, 252–266. https://doi.org/10.1093/jnci/94.4.252.
Tinsley, H.N., Gary, B.D., Keeton, A.B., Zhang, W., Abadi, A.H., Reynolds, R.C., Piazza, G. A., 2009. Sulindac sulfide selectively inhibits growth and induces apoptosis of human breast tumor cells by phosphodiesterase 5 inhibition, elevation of cyclic GMP, and activation of protein kinase G. Mol. Cancer Ther. 8, 3331–3340. https://doi.org/10.1158/1535-7163.MCT-09-0758.
Treyer, A., Mateus, A., Wiśniewski, J.R., Boriss, H., Matsson, P., Artursson, P., 2018. Intracellular drug bioavailability: effect of neutral lipids and phospholipids. Mol. Pharm. 15, 2224–2233. https://doi.org/10.1021/acs.molpharmaceut.8b00064.
Treyer, A., Walday, S., Boriss, H., Matsson, P., Artursson, P., 2019. A cell-free approach based on phospholipid characterization for determination of the cell specific unbound drug fraction (fu,cell). Pharm. Res. 36, 1–10. https://doi.org/10.1007/s11095-019-2717-1.
Tuntland, T., Ethell, B., Kosaka, T., Blasco, F., Zang, R., Jain, M., Gould, T., Hoffmaster, K., 2014. Implementation of pharmacokinetic and pharmacodynamic strategies in early research phases of drug discovery and development at novartis

institute of biomedical research. Front. Pharmacol. 5, 1–16. https://doi.org/10.3389/fphar.2014.00174.
van der Hee, B., Madsen, O., Vervoort, J., Smidt, H., Wells, J.M., 2020. Congruence of transcription programs in adult stem cell-derived jejunum organoids and original tissue during long-term culture. Front. Cell Dev. Biol. 8, 1–13. https://doi.org/10.3389/fcell.2020.00375.
Van Lieshout, E.M.M., Van Doesburg, W., Van der Meer, R., 2004. Real-time PCR of host DNA in feces to study differential exfoliation of colonocytes between rats and humans. Scand. J. Gastroenterol. 39, 852–857. https://doi.org/10.1080/00365520410006891.
Van Norman, G.A., 2019. Limitations of animal studies for predicting toxicity in clinical trials: is it time to rethink our current approach? JACC Basic Transl. Sci. 4, 845–854. https://doi.org/10.1016/j.jacbts.2019.10.008.
Van Tellingen, O., 2001. The importance of drug-transporting P-glycoproteins in toxicology. Toxicol. Lett. 120, 31–41. https://doi.org/10.1016/S0378-4274(01)00304-6.
Vandana, J.J., Manrique, C., Lacko, L.A., Chen, S., 2023. Human pluripotent-stem-cell-derived organoids for drug discovery and evaluation. Cell Stem Cell 30, 571–591. https://doi.org/10.1016/j.stem.2023.04.011.
VanDussen, K.L., Marinshaw, J.M., Shaikh, N., Miyoshi, H., Moon, C., Tarr, P.I., Ciorba, M.A., Stappenbeck, T.S., 2015. Development of an enhanced human gastrointestinal epithelial culture system to facilitate patient-based assays. Gut 64, 911–920. https://doi.org/10.1136/gutjnl-2013-306651.
Wang, D., Mann, J.R., Dubois, R.N., 2005. The role of prostaglandins and other eicosanoids in the gastrointestinal tract. Gastroenterology 128, 1445–1461. https://doi.org/10.1053/j.gastro.2004.09.080.
Williams, C.S., Watson, A.J., Sheng, H., Helou, R., Shao, J., DuBois, R.N., 2000. Celecoxib prevents tumor growth in vivo without toxicity to normal gut: lack of correlation between in vitro and in vivo models. Cancer Res. 60 (21), 6045–6051. PMID: 11085526. https://pubmed.ncbi.nlm.nih.gov/11085526/.
Wirth, T., Lafforgue, P., Pham, T., 2024. NSAID: current limits to prescription. Joint Bone Spine 91, 1–6. https://doi.org/10.1016/j.jbspin.2023.105685.
Witten, J., Samad, T., Ribbeck, K., 2019. Molecular characterization of mucus binding. Biomacromolecules 20 (4), 1505–1513. https://doi.org/10.1021/acs.biomac.8b01467.
Wright, C.W., Li, N., Shaffer, L., Hill, A., Boyer, N., Alves, S.E., Venkataraman, S., Biswas, K., Lieberman, L.A., Mohammadi, S., 2023. Establishment of a 96-well transwell system using primary human gut organoids to capture multiple quantitative pathway readouts. Sci. Rep. 13, 1–12. https://doi.org/10.1038/s41598-023-43656-z.
Xu, Z.Y., Li, J.L., 2019. Comparative review of drug–drug interactions with epidermal growth factor receptor tyrosine kinase inhibitors for the treatment of non-small-cell lung cancer. Onco. Targets Ther. 12, 5467–5484. https://doi.org/10.2147/OTT.S194870.
Xu, Y., Villalona-Calero, M.A., 2002. Irinotecan: mechanisms of tumor resistance and novel strategies for modulating its activity. Ann. Oncol. 13, 1841–1851. https://doi.org/10.1093/annonc/mdf337.
Yamashita, T., Inui, T., Yokota, J., Kawakami, K., Morinaga, G., Takatani, M., Hirayama, D., Nomoto, R., Ito, K., Cui, Y., Ruez, S., Harada, K., Kishimoto, W., Nakase, H., Mizuguchi, H., 2021. Monolayer platform using human biopsy-derived duodenal organoids for pharmaceutical research. Mol. Ther. Methods Clin. Dev. 22, 263–278. https://doi.org/10.1016/j.omtm.2021.05.005.
Yin, T., Wang, G., Ye, T., Wang, Y., 2016. Sulindac, a non-steroidal anti-inflammatory drug, mediates breast cancer inhibition as an immune modulator. Sci. Rep. 6, 1–8. https://doi.org/10.1038/srep19534.
Yoshida, S., Miwa, H., Kawachi, T., Kume, S., Takahashi, K., 2020. Generation of intestinal organoids derived from human pluripotent stem cells for drug testing. Sci. Rep. 10, 1–11. https://doi.org/10.1038/s41598-020-63151-z.
Zachos, N.C., Kovbasnjuk, O., Foulke-Abel, J., In, J., Blutt, S.E., De Jonge, H.R., Estes, M.K., Donowitz, M., 2016. Human enteroids/colonoids and intestinal organoids functionally recapitulate normal intestinal physiology and pathophysiology. J. Biol. Chem. 291, 3759–3766. https://doi.org/10.1074/jbc.R114.635995.
Zietek, T., Giesbertz, P., Ewers, M., Reichart, F., Weinmüller, M., Urbauer, E., Haller, D., Demir, I.E., Ceyhan, G.O., Kessler, H., Rath, E., 2020. Organoids to study intestinal nutrient transport, drug uptake and metabolism – update to the human model and expansion of applications. Front. Bioeng. Biotechnol. 8, 1–14. https://doi.org/10.3389/fbioe.2020.577656.